A prebiotic diet modulates microglial states and motor deficits in α-synuclein overexpressing mice

Reem Abdel-Haq[1,2], Johannes C.M. Schlachetzki[3], Joseph C. Boktor[1], Thaisa M. Cantu-Jungles[4], Taren Thron[1], Mengying Zhang[1], John W. Bostick[1], Tahmineh Khazaei[1], Sujatha Chilakala[5], Livia H. Morais[1], Greg Humphrey[6], Ali Keshavarzian[7,8], Jonathan E. Katz[5], Matt Thomson[1], Rob Knight[6,9,10,11], Viviana Gradinaru[1,2], Bruce R. Hamaker[4], Christopher K. Glass[3], Sarkis K. Mazmanian[1,2]

[1]Division of Biology and Biological Engineering, California Institute of Technology, 1200 E. California Boulevard, Pasadena, CA, 91125, USA
[2]Aligning Science Across Parkinson's (ASAP) Collaborative Research Network, Chevy Chase, MD
[3]Department of Cellular and Molecular Medicine, University of California, San Diego, La Jolla, CA
[4]Department of Food Science, Whistler Center for Carbohydrate Research, Purdue University, West Lafayette, Indiana, USA
[5]Lawrence J. Ellison Institute for Transformative Medicine, University of Southern California, Los Angeles, CA 90064, USA
[6]Department of Pediatrics, University of California, San Diego, San Diego, CA 92110, USA
[7]Department of Internal Medicine, Division of Gastroenterology, Rush University Medical Center, Chicago, IL 60612, USA
[8]Rush Center for Integrated Microbiome and Chronobiology Research, Rush University Medical Center, Chicago, IL 60612, USA
[9]Department of Computer Science and Engineering, University of California San Diego, La Jolla, CA, USA
[10]Department of Bioengineering, University of California San Diego, La Jolla, CA, USA
[11]Center for Microbiome Innovation, University of California San Diego, La Jolla, CA, USA

Correspondences to S.K.M.: sarkis@caltech.edu

Abstract

Parkinson's disease (PD) is a movement disorder characterized by neuroinflammation, α-synuclein pathology, and neurodegeneration. Most cases of PD are non-hereditary, suggesting a strong role for environmental factors, and it has been speculated that disease may originate in peripheral tissues such as the gastrointestinal (GI) tract before affecting the brain. The gut microbiome is altered in PD and may impact motor and GI symptoms as indicated by animal studies, though mechanisms of gut-brain interactions remain incompletely defined. Intestinal bacteria ferment dietary fibers into short-chain fatty acids, with fecal levels of these molecules differing between PD and healthy controls and in mouse models. Among other effects, dietary microbial metabolites can modulate activation of microglia, brain-resident immune cells implicated in PD. We therefore investigated whether a fiber-rich diet influences microglial function in α-synuclein overexpressing (ASO) mice, a preclinical model with PD-like symptoms and pathology. Feeding a prebiotic high-fiber diet attenuates motor deficits and reduces α-synuclein aggregation in the substantia nigra of mice. Concomitantly, the gut microbiome of ASO mice adopts a profile correlated with health upon prebiotic treatment, which also reduces microglial activation. Single-cell RNA-seq analysis of microglia from the substantia nigra and striatum uncovers increased pro-inflammatory signaling and reduced homeostatic responses in ASO mice compared to wild-type counterparts on standard diets. However, prebiotic feeding reverses pathogenic microglial states in ASO mice and promotes expansion of protective disease-associated macrophage (DAM) subsets of microglia. Notably, depletion of microglia using a CSF1R inhibitor eliminates the beneficial effects of prebiotics by restoring motor deficits to ASO mice despite feeding a prebiotic diet. These studies uncover a novel microglia-dependent interaction between diet and motor symptoms in mice, findings that may have implications for neuroinflammation and PD.

Introduction

Parkinson's disease (PD) is the second most common neurodegenerative disorder in the United States and affects ~1% of the population over the age of 65. The incidence rate of PD is projected to double between 2015 and 2040, mainly due to lifestyle factors and increased lifespan (Dorsey et al. 2018). Clinical features of PD include slowed movement, muscle rigidity, resting tremors, and postural instability. These symptoms result from death of dopaminergic neurons of the nigrostriatal pathway regulating motor function (Poewe et al. 2017). Abnormal aggregation of the neuronal protein α-synuclein (αSyn) promotes disruptions in multiple cellular processes that contribute to neurodegeneration, including mitochondrial dysfunction, oxidative stress, proteasomal impairment, autophagy deficits, and neuroinflammation (Poewe et al. 2017).

Although PD is predominantly classified as a brain disorder, 70-80% of patients experience gastrointestinal (GI) symptoms, mainly constipation but also abdominal pain and increased intestinal permeability that usually manifests in the prodromal stages (Forsyth et al. 2011; Yang et al. 2019). Braak's hypothesis postulated nearly 20 years ago that αSyn aggregation may start at peripheral environmental interfaces, like the GI tract or olfactory bulb, and eventually reach the brain stem, substantia nigra, and neocortex via the vagus nerve (Braak et al. 2003). Increasing evidence has corroborated the potential for gut-to-brain spread of αSyn pathology in rodents (S. Kim et al. 2019; B. Liu et al. 2017; Svensson et al. 2015). Additionally, several studies have detected differences in gut microbiome composition between PD patients and healthy controls (Çamcı and Oğuz 2016; Keshavarzian et al. 2015; Scheperjans et al. 2015; A. H. Tan et al. 2014), with decreased abundance of health-promoting bacteria and an increase in pro-inflammatory pathogenic bacteria in the PD microbiome. Altering the microbiome in α-synuclein overexpressing (ASO) mice modulates brain pathology and motor performance (Sampson et al. 2016), and gut bacterial species have been shown to accelerate disease in other PD mouse models (Choi et al. 2018; Sampson et al. 2020). Additionally, antibiotic treatment improves motor symptoms in several models of PD (Cui et al. 2022; Pu et al. 2019; Sampson et al. 2016).

One potential target of gut-brain signaling in PD are microglia, a highly dynamic population of brain cells that can shape neural circuity through regulation of neurogenesis, synaptic pruning, and myelination (Anderson and Vetter 2019). In PD and other neurodegenerative conditions,

84 microglial cellular repair responses are thought to become dysregulated, ultimately resulting in
85 heightened reactivity and chronic inflammation that drives neurodegeneration (Troncoso-
86 Escudero et al. 2018). Microglia not only sense signals from within the brain but also receive
87 input from the periphery, including the gut microbiome (Abdel-Haq et al. 2019). Offspring of
88 germ-free (GF) mice show differences in microglial gene expression and chromatin accessibility
89 compared to specific-pathogen-free (SPF) counterparts (Thion et al. 2018). Microglia from adult
90 GF mice present an immature gene expression profile and fail to adequately respond to
91 immunostimulants (Erny et al. 2015; Thion et al. 2018). However, feeding GF mice a mixture of
92 short-chain fatty acids (SCFAs), metabolic products of bacterial fiber fermentation, is sufficient
93 to rescue microglial maturation (Erny et al. 2015). Interestingly, levels of SCFAs are reduced in
94 fecal samples from PD patients compared to matched controls (Chen et al. 2022; Unger et al.
95 2016) and inversely correlate with disease severity (Aho et al. 2021; Chen et al. 2022).
96
97 Herein, we explore the interplay between diet and microglia in the ASO mouse model, which
98 recapitulates many of the hallmark symptoms of PD including motor deficits, GI abnormalities,
99 olfactory dysfunction, and neuroinflammation (Chesselet et al. 2012). We demonstrate that a
100 prebiotic diet remodels the gut microbiome of ASO mice to adopt a protective profile. Prebiotic
101 intervention attenuates motor deficits and reduces αSyn aggregates in the substantia nigra of
102 ASO mice in a microglia-dependent manner. Prebiotic diet alters the morphology and gene
103 expression patterns of microglia in brain regions involved in PD, promoting phenotypes
104 associated with disease-protective responses. Importantly, microglial depletion abrogates the
105 beneficial effects of prebiotics. Overall, this study reveals that enhanced metabolism of dietary
106 fiber by the gut microbiome alters the physiology of cells in the central nervous system (CNS)
107 and ultimately improves behavioral and pathologic outcomes in a mouse model of PD.
108
109 **Results**
110 **Prebiotic diet attenuates motor symptoms and reduces αSyn aggregation in the brain**
111 We generated three custom high-fiber diets **(Supplement Table 1)**, each containing 20% of a
112 prebiotic mixture of two or three dietary fibers designed to promote growth of distinct gut
113 bacterial taxa **(Supplement Figure 1A)** and boost SCFA production (**Supplement Figure 1B-E)**
114 based on *in vitro* fecal fermentation. The prebiotic diets **(Supplement Figure 1F)** were

compared to a cellulose-free control diet that is similar in major micro- and macro-nutrients **(Supplement Table 1)**.

We fed each of the three prebiotic diets (prebiotic #1, #2, #3) to male ASO mice from 5-22 weeks of age. To assess whether long-term prebiotic intervention ameliorated motor deficits, mice were subjected to a battery of motor tests to evaluate fine motor control, grip strength, locomotion, and coordination **(Figure 1A-D, Supplement Figure 2A-G)**. We identified a single prebiotic (prebiotic #1, referred to hereafter as "prebiotic") that improved disease symptoms in ASO mice. Remarkably, administration of the prebiotic diet to ASO mice enhanced performance in several motor behavioral tests, including the pole descent and beam traversal tests (time to cross, steps to cross, errors per step) compared to mice fed a control diet **(Figure 1A-D).** Outcomes in other paradigms including adhesive removal, wire hang, and hindlimb score were unchanged **(Supplement Figure 3A-C)**. These findings reveal that a gut-targeting intervention has the potential to attenuate key behavioral features in a mouse model of PD.

As anticipated, levels of all major SCFAs were higher in fecal samples from prebiotic-fed mice than from control-fed mice **(Figure 1E)**. Interestingly, concentrations of propionate, butyrate, and isobutyrate were not significantly different between wild type (WT) and ASO mice fed a control diet **(Figure 1E)**. ASO mice weighed significantly less than their WT counterparts and exhibited reduced food intake of control diet, but not prebiotic diet **(Supplement Figure 3D-E).** While prebiotic-ASO mice ate significantly more than control-ASO mice, no difference in body weight was detected between the groups at 22 weeks of age **(Supplement Figure 3D)**. There were no obvious health issues in animals on either diet.

Aggregation of αSyn is a hallmark of PD pathology. We found a significant reduction in αSyn aggregation in the substantia nigra (SN) of prebiotic-fed ASO mice compared to ASO mice on control chow **(Figure 1F).** In contrast, prebiotic intervention had no effect on αSyn aggregation in the striatum (STR) **(Figure 1G).** We speculate that this difference may be attributable to regional differences in microglia density, gene expression, and clearance activity, with the SN having a relatively higher density of microglia (Grabert et al. 2016; Y.-L. Tan, Yuan, and Tian

2020). Taken together, these results suggest that early intervention with a prebiotic diet can reduce PD-like symptoms and brain pathology in ASO mice.

Prebiotics alter gut microbiome composition

Gut microbiome composition is strongly influenced by diet in mice and humans (Turnbaugh et al. 2009; Wu et al. 2011). We performed shotgun metagenomics on fecal samples from mice fed control or prebiotic diet. Alpha diversity analysis revealed significant reduction in observed species count, Shannon's diversity, and Simpson's evenness in prebiotic-fed groups, as well as an increase in Gini's dominance **(Figure 2A-D)**. This is consistent with a previous report of reduced microbiome diversity in high-fiber fed mice (Luo et al. 2017). Principal coordinate analysis (PCoA) of species abundance showed that samples clustered more closely by diet than mouse genotype (**Figure 2E)** and PERMANOVA revealed that prebiotic treatment explained 6-fold more variance than genotype, with R^2 values of 0.334 and 0.053 for each, respectively **(Figure 2F)**. Thus, the prebiotic diet reshapes gut microbial communities in WT and ASO mice.

We observed broad changes at the microbial phylum and genus levels following administration of prebiotic diet **(Figure 2G, I)**, displaying an increase in Bacteroidetes and a decrease in Firmicutes in prebiotic diet-fed mice, resulting in a lower Firmicutes/Bacteroidetes (F/B) ratio that has been associated with general features of metabolic health **(Figure 2H)**. Intriguingly, it has been shown that Bacteroidetes are reduced in PD patients compared to age-matched controls, suggesting the prebiotic may counter this effect (Unger et al. 2016). Additionally, we observed a decrease in Proteobacteria, a phylum often increased in dysbiosis and inflammation and elevated in PD patient fecal samples **(Figure 2H)** (Keshavarzian et al. 2015; Shin, Whon, and Bae 2015). Gut-brain module analysis showed variation in metabolic pathways including SCFA degradation/synthesis in response to diet and genotype **(Figure 2J)**. Overall, feeding of a prebiotic diet appears to qualitatively restructure the ASO microbiome toward an anti-inflammatory and potentially protective profile.

Prebiotic diet alters microglia morphology in ASO mice

In ASO mice, microglia reactivity in response to αSyn overexpression appears at 4-5 weeks of age in the STR and at 20-24 weeks of age in the SN (Watson et al. 2012). SCFAs have been

shown to influence the physiology of microglia in several contexts (Colombo et al. 2021; Erny et al. 2015; Sadler et al. 2020; Erny et al. 2021; Sampson et al. 2016). To explore whether prebiotics alter microglia morphology, we performed immunofluorescence imaging using the pan-microglial marker IBA1. The morphology of microglia can indicate their reactivity state, with homeostatic microglia exhibiting a ramified shape with a smaller cell body and increased dendritic processes, whereas activated microglia adopt an amoeboid form with a larger cell body and retracted processes (Menassa and Gomez-Nicola 2018). We observed that microglia in the SN and STR of prebiotic-ASO mice had significantly smaller cell bodies than in control-ASO mice (**Figure 3A-B)**. 3D analysis of key morphological features revealed that microglia in the SN and STR of prebiotic-ASO mice exhibited increased dendrite length, number of segments, number of branch points, and number of terminal points compared to microglia from control-ASO mice **(Figure 3C-F).** Taken together, these findings indicate that long-term prebiotic intervention dampens microglial reactivity in brain regions implicated in PD.

ASO mice display increased disease-promoting microglial subsets

Single cell RNA sequencing (scRNA-seq) has emerged as a powerful tool to interrogate microglial biology in mouse models of neurodegeneration (Keren-Shaul et al. 2017; W. Liu et al. 2020). We first sought to investigate differences in microglial gene expression between control-WT and control-ASO mice (no prebiotics), since scRNA-seq of microglia has not been previously applied to this mouse model. Differential gene expression analysis of all cells revealed 313 differentially expressed genes (DEGs) (↑163, ↓150, FDR<0.05) in the SN and 997 DEGs (↑511, ↓486) in the STR. In the SN, microglia harvested from control-ASO mice displayed increased expression of MHC class I components (*H2-K1, H2-D1*), several chemokines (*Ccl2, Ccl3, Ccl4, Ccl9*) and chemokine receptors (*Ccr1, Ccr5*), and pro-inflammatory markers (*Nfkbid, CD74*) **(Figure 4C, Supplement Table 2)**. Gene enrichment analysis of all upregulated DEGs in control-ASO mice showed enrichment in pathways related to cellular responses to cytokine stimulus and interferon-gamma, immune system processes, and response to stress **(Figure 4D)**. Interestingly, several genes that were downregulated in control-ASO mice compared to control-WT were related to anti-inflammatory signaling (*Klf2, Klf4*) and microglial homeostasis (*P2ry12, Slc2a5*) **(Figure 4C, Supplement Table 2)**. We observed similar trends in the STR, with control-ASO microglia upregulating pro-inflammatory

modulators (*Tnf, Nfkbiz, Trim8, Irgm1*) and antigen processing and presentation genes (*H2-Q7, H2-K1*, *H2-D1*, *H2-T23*) and downregulating genes related to homeostatic cellular processes **(Figure 4H-I, Supplement Table 4)**. Notably, the anti-inflammatory cytokine transforming growth factor beta 2 (*Tgfβ2*) was ~45-fold downregulated in control-ASO **(Supplement Table 4)**. These data suggest microglia from control-ASO mice upregulate pro-inflammatory immune processes and downregulate pathways related to homeostasis and cellular maintenance in response to αSyn overexpression.

Prebiotic diet promotes microglia with disease-protective functions

Based on global scRNA-seq gene expression, Uniform Manifold Approximation and Projection for Dimension Reduction (UMAP) analysis yielded nine distinct microglia clusters in the SN and eight clusters in the STR **(Figure 4A, F)**. In the SN, we detected differences in cluster distribution between experimental groups, with the strongest differences in clusters 0 and 2 **(Figure 4A-B)**. Interestingly, the percentage of microglia in cluster 0 was higher in control-ASO than control-WT mice (27.1% vs. 18.9%), and prebiotic treatment reduced the percentage of microglia belonging to cluster 0 in ASO mice compared to control diets (18.3%) **(Figure 4B)**. Gene enrichment analysis of the top 50 genes associated with cluster 0 revealed pathways related to immune system processes, cellular response to tumor necrosis factor (TNF), cellular response to lipopolysaccharide, and response to stress. Cluster 0 contained several prominent immune markers including *Tnf, Nfkbia, Ccl2, Ccl3,* and *Ccl4,* suggesting that a prebiotic diet may suppress or prevent pro-inflammatory responses in ASO mice. Notably, levels of TNF and Ccl2 are elevated in the serum of PD patients (Brodacki et al. 2008; Reale et al. 2009). Conversely, the percentage of microglia belonging to cluster 2 was reduced in control-ASO mice but increased in prebiotic-ASO mice **(Figure 4B)**. Among the most highly expressed genes in cluster 2 were the homeostatic microglial markers *P2ry12* and *Cst3,* as well as the anti-inflammatory transcription factors *Klf2* and *Klf4* (Das et al. 2006; Li et al. 2018).

Within the STR, we detected eight clusters of microglia, with notable shifts in clusters 1 and 3 **(Figure 4F-G)**. The top 10 associative genes in cluster 3 included several mitochondrial genes*: mt-Atp6, mt-Cytb, mt-Co2, mt-Co3, mt-Nd4, mt-Nd1,* and *mt-Nd2*. Additionally, we detected a 13.4% increase in cluster 1 in control-ASO mice, with prebiotic diet restoring the percentage of

cluster 1 back to control-WT levels **(Figure 4G)**. The significantly enriched pathways within cluster 1 included those positively regulating cell death and immune system development, and negatively regulating cellular processes, suggesting increased immune signaling and dysregulation of homeostatic signaling in the absence of prebiotic treatment.

To determine effects of long-term prebiotic exposure on microglial gene expression in ASO mice, we compared prebiotic-ASO microglia to control-ASO and found 473 DEGs (↑317, ↓156) in the SN and 1,474 DEGs (↑608, ↓866) in the STR **(Figure 4C, H, Supplement Tables 3, 5).** Gene enrichment analysis of the 156 genes downregulated in prebiotic-ASO microglia in the SN revealed reduction in interleukin-1 (IL-1)β production pathways, as well as dampened innate immune response and defense response pathways compared to control-ASO mice **(Figure 4E)**. Among the genes downregulated in microglia from prebiotic-ASO mice were several mediators of the pro-inflammatory immune response (*Mif, Masp1, Trim12a, Bs2, B2m*), antigen presentation and processing (*H2-Q7*), and chemokines/receptors (*Ccl9, Ccr1, Ccr5*) **(Figure 4C, Supplement Table 3)**. We observed a similar trend in the STR, with prebiotic-ASO showing downregulation of pathways related to innate immunity, response to stress, and defense response **(Figure 4H, J, Supplement Table 5)**. Interestingly, several of the pro-inflammatory markers upregulated in control-ASO and downregulated in prebiotic-ASO microglia were expressed by a small subset of microglia, suggesting that a subpopulation of cells alters its transcriptomic profile in response to αSyn expression, similar to what has been observed in microglia from aged mice and a mouse model of Alzheimer's disease (AD) (Hammond et al. 2019; Keren-Shaul et al. 2017). Further DEG analysis revealed increased expression of several markers that define disease-associated macrophages (DAM) in the SN and STR in prebiotic-ASO mice **(Supplement Tables 3, 5)**, a microglial sub-population associated with protection during early stages of disease in several mouse models (Deczkowska et al. 2018; Onuska 2020). Notably, we observed an increase in Trem2 in microglia from the STR of prebiotic-ASO mice, suggesting prebiotics may induce a neuroprotective DAM phenotype by 22 weeks of age (Gratuze, Leyns, and Holtzman 2018; Keren-Shaul et al. 2017; Onuska 2020). Taken together, gene expression analysis suggests prebiotic intervention in ASO mice dampens proinflammatory and neurotoxic signaling pathways and potentially upregulates a neuroprotective phenotype in microglia.

Potential effects of SCFAs are likely indirect and not via epigenetic regulation

We detected no differences in SCFA levels between control and prebiotic animal groups in either the SN or STR **(Supplement Figure 4A-B)**. SCFAs can signal through activation of GPCR receptors (GPCR43 or FFAR2, and GPCR41 or FFAR3) and/or inhibition of histone deacetylases (HDACs), altering the epigenetic landscape of target cells (Silva, Bernardi, and Frozza 2020; Vinolo et al. 2011). As determined via qRT-PCR, ASO mice exhibited very low or no expression of FFAR2 and FFAR3 in the cerebellum, midbrain, striatum, motor cortex relative to the small intestine **(Supplement Figure 5A, B),** consistent with scRNA-seq data showing an absence of FFAR2/3 expression in microglia in the SN and STR **(Supplement Table 6)**.

To explore whether the prebiotic diet was inducing epigenetic changes, we performed bulk ATAC-seq on purified microglia from the SN and STR and observed no significant differences in chromatin accessibility between experimental groups **(Supplement Figure 5C, D)**. However, from this bulk measurement, we cannot rule out changes in open chromatin or histone modifications in specific subset(s) of microglia. We also measured the expression levels of several HDAC isoforms (*HDAC 1,2,6,7, and 9*) in the striatum and found no differences in expression between control and prebiotic groups of both genotypes **(Supplement Figure 5E-I)**. Collectively, these findings suggest that dietary metabolites may influence microglial gene expression through indirect mechanisms and likely not by entering the brain, consistent with previous reports (Erny et al. 2015), though additional work is needed to validate this hypothesis.

Depletion of microglia blocks beneficial effects of prebiotics

Microglia are dependent on colony stimulating factor 1 receptor (CSF1R) signaling for development, maintenance, and proliferation (Elmore et al. 2014). PLX5622 is a brain-penetrant inhibitor of CSF1R that can deplete microglia with no observed effects on behavior or cognition (Elmore et al. 2014). We added PLX5622 to the diet of mice from 5-22 weeks of age, and quantified the number of IBA1+ microglia in various brain regions. The efficiency of microglial depletion varied depending on brain region, with regions containing low numbers of microglia such as the cerebellum exhibiting higher depletion (~80%) than areas with high microglial density such as the SN (~65%) and STR (~75%) **(Figure 5A-C).** We did not observe differences

in depletion efficiency between WT and ASO mice or between control and prebiotic-fed mice **(Supplement Figure 6A-B)**.

Following PLX5622 treatment, we assayed motor behavior at 22 weeks of age. PLX5622 treatment had no impact on motor performance in tests where prebiotic treatment had no effect **(Supplement Figure 6C-F).** Remarkably however, even incomplete microglia depletion eliminated prebiotic-induced improvements in the pole descent and beam traversal tests (time to cross, errors per step) **(Figure 5D-F)**, suggesting that microglia are required for the ability of prebiotics to ameliorate motor deficits. PLX5622 treatment did not alter body weight in control or prebiotic-fed mice **(Supplement Figure 6G)**. We also measured αSyn aggregation in the SN and STR of 22-week-old mice. In control-fed mice, depletion of microglia had no impact on levels of αSyn aggregation in the SN or STR **(Figure 5G-H).** However, in prebiotic-fed ASO mice, depletion of microglia significantly increased levels of aggregated αSyn in the SN, while levels in the STR remained unchanged **(Figure 5G-H)**. These data reveal that partial ablation of microglia or diminished CSF1R signaling eliminate the protective effects of the prebiotic diet in ASO mice.

While previous studies have characterized the effect of PLX5622 on macrophages in the spleen and bone marrow (Lei et al. 2020), knowledge of the effect of this drug on immune cell populations in the GI tract of mice is largely unexplored. Surprisingly, most gut-associated immune cell populations were unaffected by PLX5622 treatment. In the large intestine, PLX5622 treatment caused a reduction in $CD45^{+}$ $CSF1R^{lo}$ lymphocytes, but had no impact on $CD45^{+}$ $CSF1R^{hi}$ cells, pan T cells or B cells **(Supplement Figure 7A-E).** In the small intestine, levels of these cell types were unchanged in response to PLX5622 **(Supplement Figure 7F-J)**. In the spleen, while $CSF1R^{lo}$ lymphocytes were reduced in Prebiotic + PLX5622 mice, levels of $CSF1R^{hi}$ macrophages were significantly elevated in Control + PLX5622 and Prebiotic + PLX5622 mice, suggesting a potential compensatory mechanism in this organ **(Supplement Figure 7K-O)**. These findings point to a relatively high specificity of CSF1R-targeted depletion in the brain, further implicating microglia as a key mediator of the beneficial effects of prebiotic treatment in ASO mice.

Discussion

We describe how administering a prebiotic diet to α-synuclein overexpressing mice results in improved motor performance with reduced microglial reactivity and αSyn pathology. The mechanism by which a high-fiber diet influences microglial physiology and alters behavior remains unclear. SCFA levels in the brain tissue of prebiotic-fed mice were unchanged, and our data suggest that SCFAs do not appear to signal through known GPCRs in the brain or via epigenetic remodeling of microglia-derived chromatin, further reinforcing the notion of indirect effects on microglia, as previously suggested (Erny et al. 2015). SCFAs are known to have immune modulatory properties in the gut (Parada Venegas et al. 2019), among other functions, and we speculate that altering peripheral immunity may affect microglial reactivity states and gene expression. We note that it is possible molecules other than SCFAs may be contributing to prebiotic-induced changes in microglial physiology, a notion we are unable to test in the ASO mouse model.

Studies of SCFAs in preclinical models paint a complex picture, with varying outcomes in germ-free (GF) vs. SPF settings. Oral administration of SCFAs to GF mice induces microglial reactivity in wild-type mice (Erny et al. 2015), a mouse model of AD (Colombo et al. 2021), and ASO mice, where feeding the metabolites in the absence of gut bacteria exacerbates motor deficits and neuroinflammation (Sampson et al. 2016). In contrast, two independent studies found that sodium butyrate treatment alleviates motor deficits and reduces microglial reactivity in 1-methyl-4-phenyl-1,2,3,6-tetrahydropyridine (MPTP) mice with a laboratory microbiota (Hou et al. 2021; J. Liu et al. 2017). Our findings underscore the need to consider context (GF vs. SPF), diet, and form and duration of intervention in future diet studies in mouse models.

Microglia have been increasing linked to neurodegenerative disorders and PD. Depletion of microglia using CSF1R inhibitors confers deleterious effects in certain mouse models of PD **(**MPTP, human α-Syn AAV) (George et al. 2019; X. Yang et al. 2018), LPS-induced sickness behavior (Vichaya et al. 2020), and prion disease (Carroll et al. 2018). In contrast, microglia depletion improves disease outcome in experimental autoimmune encephalomyelitis (EAE), a preclinical models of multiple sclerosis (Nissen et al. 2018), and in the 3xTg and 5xFAD mouse models of AD (Casali et al. 2020; E. E. Spangenberg et al. 2016; E. Spangenberg et al. 2019).

Herein, we found that depletion of microglia neither exacerbates nor improves motor performance in naïve (control diet) mice, suggesting that microglia do not influence behavior in ASO mice, at least in the early stages of disease progression. In contrast, the protective effects of a prebiotic diet do require microglia since their depletion eliminated improvements in motor behavior and αSyn pathology in the brain.

We extended these findings with scRNA sequencing, uncovering functional effects including prebiotic-mediated restoration of pathways known to be dysregulated in PD including inflammation and homeostatic cellular functions. Moreover, we found that prebiotic intervention significantly increases CSF1 expression in ASO microglia in both the SN and STR, potentially implicating CSF1 signaling pathways in mediating the protective effects of prebiotics. Further insights into how prebiotic diets modulate microglia biology and how these events translate into amelioration of motor symptoms and brain pathology await future research. Microglia have been shown to present a distinct transcriptomic profile and respond to various environmental factors, including the microbiome, in a sex-specific manner (Thion et al. 2018; Villa et al. 2018). While this study probed the effects of prebiotics on microglia in male mice, additional insight may come from similar investigation of female animals.

Prebiotics present a potentially promising therapeutic approach as diet is a significant contributor to microbiome composition and epidemiological evidence has linked high-fiber diets with reduced risk of developing PD (Boulos et al. 2019). While increased intake of fruits, vegetables, and adherence to a Mediterranean diet are associated with a lower risk of PD, individuals consuming a low-fiber, highly-processed Western diet exhibit an increased risk of PD diagnosis (Alcalay et al. 2012; Gao et al. 2007; Molsberry et al. 2020). Several ongoing clinical trials are exploring the beneficial effects of probiotics and prebiotics on PD-related outcomes. Gut-targeted therapies offer several advantages compared to traditional therapeutic approaches for brain disorders. Conventional pharmacological treatments rely on chemicals which may lose efficacy over time, often fail to treat underlying pathophysiology, and may result in undesirable side effects for the patient. A notable challenge for CNS-targeting drugs is delivery, requiring drugs that can efficiently cross the blood-brain barrier. Harnessing safe and practical treatment options based on diet may therefore help accelerate novel therapeutics for PD.

Figure Legends

Figure 1. Prebiotic diet attenuates motor symptoms and reduces αSyn aggregation

A-D) Motor behavior metrics at 22 weeks of age for prebiotic- and control-fed WT and ASO mice from pole descent (B) and beam traversal (C-E) tests. Motor test data is derived from two independent experiments (n=16-29/group). **E)** Concentrations (μM) of acetate, propionate, butyrate, and isobutyrate in fecal samples collected from prebiotic-fed WT and ASO mice (n=7-12/group). **F-G)** Aggregated α-synuclein levels in the substantia nigra (SN) (F; n=8-10/group) and striatum (STR) (G; n=9-11/group) measured by dot blot. Each point represents data from one mouse. Data analyzed by two-way ANOVA followed by Tukey's multiple comparisons test. Bars represent mean ± SEM. *p<0.05, **p<0.01, ***p<0.001, and ****p<0.0001.

Figure 2. Prebiotic diet alters gut microbiome composition

A-D) Diversity metrics from metagenomic analysis of treatment groups at 22 weeks of age, including observed species count (A), Shannon's diversity (B), Simpson's evenness (C), and Gini's dominance (D). **E)** Principal Coordinate Analysis (PCoA) plot of Bray-Curtis dissimilarity (n=12-25/group). **F)** PERMANOVA analysis summary of Bray-Curtis dissimilarity. **G)** Relative abundance of phyla among treatment groups (left) and heat map showing differentially abundant phyla (right). Diet values are displayed relative to control diet and genotype values relative to WT mice. **H)** Relative abundance of select phyla in treatment groups. **I)** Summary plot of relative abundance of genera. **J)** Differentially expressed pathways identified from the "Gut Microbiome-Brain module". Diet values are displayed relative to control diet and genotype values relative to WT mice (n=12-25/group).

Figure 3. Prebiotic diet alters microglia morphology and reactivity status in ASO mice

A,B) Measurement of IBA1+ microglia diameter in substantia nigra (SN) (A; n=5/group) and striatum (STR) (B; n=5/group). Left: quantification of cell diameter. Each point represents one mouse with 26-79 cells measured per mouse. Right: Representative 20x images of IBA1+ staining. Scale bars 50 μm. **C-F)** 3D reconstruction of microglia in the substantia nigra (C-D) and striatum (E-F). C,E) Quantification of dendrite length, number of segments, number of branch points, and number of terminal points (n=14-18/group for SN and n=12-14/group for STR). Each point represents one cell, with 3-5 cells analyzed/mouse. D,F) representative 3D

reconstructions of microglia imaged at 40x magnification. Data analyzed by two-way ANOVA followed by Tukey's multiple comparisons test. Bars represent mean ± SEM. *p<0.05, **p<0.01, ***p<0.001, and ****p<0.0001.

Figure 4. Prebiotic diet alters microglial gene expression

A) UMAP plot of all 5,278 substantia nigra (SN) cells sequenced by scRNA-seq from all four treatment groups (left) and distribution of cells from individual samples (right). **B)** Relative distribution of cells within each cluster in the SN. **C)** Dot plot showing genes significantly upregulated in control-ASO microglia (relative to control-WT) and significantly downregulated in prebiotic-ASO microglia (relative to control-ASO) in the SN. **D)** Significantly enriched pathways among 163 genes upregulated in control-ASO microglia relative to control-WT microglia in the SN. **E)** Significantly enriched pathways among 156 genes downregulated in prebiotic-ASO microglia relative to control-ASO microglia in the SN. **F)** UMAP plot of all 27,152 striatal (STR) cells sequenced by scRNA-seq from all four treatment groups (left) and distribution of cells from individual samples (right). **G)** Relative distribution of cells within each cluster in the STR. **H)** Dot plot and showing genes significantly upregulated in control-ASO microglia (relative to control-WT) and significantly downregulated in prebiotic-ASO microglia (relative to control-ASO) in the STR. **I)** Significantly enriched pathways among the 50 most upregulated genes in control-ASO microglia relative to control-WT microglia in the STR. **J)** Significantly enriched pathways among the 50 most downregulated genes in prebiotic-ASO microglia relative to control-ASO microglia in the STR.

Figure 5. Depletion of microglia inhibits beneficial effects of prebiotics

A-C) Number of IBA1+ cells per field of view in 20X images of the cerebellum (A), substantia nigra (B), and striatum (C). n=4/group. Representative images from the striatum are shown at right (scale bars: 50 μm). **D-F)** Motor performance metrics for pole descent (D) and beam traversal (E-F) tests. Motor data derived from five independent cohorts (n=12-21/group). **G,H)** Aggregated α-synuclein measured by dot blot in the substantia nigra (G; n=6-10/group) and striatum (H; n=6-8/group). Microglia count data analyzed by one-way ANOVA followed by Tukey's multiple comparisons test. Motor and αSyn data analyzed by two-way ANOVA

454 followed by Tukey's multiple comparisons test. Data represent mean ± SEM. *p<0.05,
455 **p<0.01, ***p<0.001, and ****p<0.0001.
456
457 **Supplement Figure 1. Effect of dietary fibers on gut microbial community and metabolic**
458 **function *in vitro***
459 **A)** Hierarchical clustering of the 25 most abundant genera after 24 h of *in vitro* fecal
460 fermentation using a pooled human gut microbiota community, as previously described (Cantu-
461 Jungles et al. 2018). Taxa were associated with fiber type by hierarchical clustering using
462 Euclidean distances and the Ward algorithm. **B-D)** SCFA concentration (mM) in fecal slurries of
463 acetate (B), butyrate (C) and propionate (D). Data analyzed by two-way ANOVA followed by
464 Tukey's multiple comparisons test. Statistical differences from the blank are indicated by
465 *p<0.05, **p<0.01, ***p<0.001, and ****p<0.0001. **E)** Relative proportion of each SCFA
466 produced in the 24 h *in vitro* fecal fermentation, showing association with fiber type. **F)** Fiber
467 composition of Prebiotic Diets 1-3.
468
469 **Supplement Figure 2. Motor behavior in mice fed Prebiotic #2 and Prebiotic #3 diets**
470 **A-D)** Motor behavior metrics for mice fed Prebiotic #2 diet from beam traversal (A,B), wire
471 hang (C), and adhesive removal (D) tests. **E-G)** Motor behavior metrics for mice fed Prebiotic #3
472 diet from wire hang (E), adhesive removal (F), and hindlimb score (G) tests (n=6-7/group). Data
473 analyzed by two-way ANOVA followed by Tukey's multiple comparisons test, except for
474 hindlimb score data, which was analyzed by Kruskal-Wallis test. Bars represent mean ± SEM.
475 *p<0.05, **p<0.01, ***p<0.001, and ****p<0.0001.
476
477 **Supplement Figure 3. Prebiotic diet does not improve performance in certain motor tests**
478 **A-C)** Motor behavior metrics for mice at 22 weeks from wire hang (A), adhesive removal (B),
479 and hindlimb score (C) tests (n=18-24/group). **D)** Mouse weight at 22 weeks (n=16-24/group).
480 **E)** Food intake per mouse recorded over the course of experiment. Data analyzed by two-way
481 ANOVA followed by Tukey's multiple comparisons test, except hindlimb score data, which was
482 analyzed by Kruskal-Wallis test. Bars represent mean ± SEM. *p<0.05, **p<0.01, ***p<0.001,
483 and ****p<0.0001.
484

Supplement Figure 4. Prebiotics do not change SCFA levels in the brain

A,B) Concentration (μM) of acetate, propionate, and butyrate measured by UHP-LC in the substantia nigra (A) and striatum (B). Each point represents data from one mouse (n=5/group). Data analyzed by two-way ANOVA followed by Tukey's multiple comparisons test. Bars represent mean ± SEM.

Supplement Figure 5. FFAR2/3 levels in brain and GI tissue and epigenetic analysis

A,B) qPCR measurement of FFAR2 (A) and FFAR3 (B) in small intestine, cerebellum, midbrain, striatum and motor cortex (n=2-4/group). **C,D)** ATAC-seq measurement of open chromatin regions in purified microglia in the substantia nigra (C) and striatum (D). **E-I)** qPCR measurement of HDAC-1 (E), HDAC-2 (F), HDAC-6 (G), HDAC-7 (H), and HDAC-9 (I) in the striatum (n=5-6/group). qPCR data analyzed by two-way ANOVA followed by Tukey's multiple comparisons test. Bars represent mean ± SEM. *p<0.05, **p<0.01, ***p<0.001, and ****p<0.0001.

Supplement Figure 6. Characterization of PLX5622 treatment

A,B) Iba1+ cell count in the substantia nigra (A) and striatum (B). n=2/group. **C-F)** Motor behavior metrics from beam traversal (C), wire hang (D), hindlimb score (E), and adhesive removal (F) tests (n=12-23/group). **G)** Mouse weight at 22 weeks (n=9-15/group). Data analyzed by two-way ANOVA followed by Tukey's multiple comparisons test. Bars represent mean ± SEM. *p<0.05, **p<0.01, ***p<0.001, and ****p<0.0001.

Supplement Figure 7. Immune cell characterization in the gut and spleen of PLX5622-treated mice

A-E) Large intestine quantification of CD45, CSF1r+ high cells (A); CD45+, CSF1r low cells (B); CD11b+, CD45 high cells (C); T cells (CD19-, CD3e+) (D); and B cells (CD19+, CD3e-) (E). n=6-8/group. **F-J)** Small intestine quantification of the same populations (n=6-8/group). **K-O)** Spleen quantification of the same populations (n=3-6/group). Each point represents data from an individual mouse. White data points represent WT mice and grey data points represent ASO mice. Data is combined from three independent experiments. Data analyzed by one-way

ANOVA followed by Tukey's multiple comparisons test. Bars represent mean ± SEM. *p<0.05, **p<0.01, ***p<0.001, and ****p<0.0001.

Supplement Table 1. Composition of custom-made prebiotic diets

Supplement Table 2. DEGs in Control-WT vs Control-ASO microglia in the Substantia Nigra
Log fold change relative to Control-WT

Supplement Table 3. DEGs in Control-ASO vs Prebiotic-ASO microglia in the Substantia Nigra
Log fold change relative to Control-ASO

Supplement Table 4. DEGs in Control-WT vs Control-ASO microglia in the Striatum
Log fold change relative to Control-WT

Supplement Table 5. DEGs in Control-ASO vs Prebiotic-ASO microglia in the Striatum
Log fold change relative to Control-ASO

Supplement Table 6. Gene detected in microglia in scRNA-seq in the Substantia Nigra and Striatum

Materials and Methods

Animals

Breeding: The Thy1-α-synuclein (ASO; line 61) mouse line was used for all experiments in this study (Chesselet et al. 2012; Rockenstein et al. 2002). Male BDF1 mice were crossed with female ASO mice expressing the α-synuclein transgene on the X chromosome to generate WT and ASO littermates. Mice were weaned at p21 and housed by genotype on the day of weaning. Male mice were used for all experiments in this study.

Diet experiments: Mice were switched from standard chow to either the cellulose-free control diet or high-fiber prebiotic diet at 5-6 weeks of age and housed in sterile, autoclaved cages with sterile water. Custom fiber mixes were sent from Purdue University for formulation at Envigo Teklad (Madison, WI, USA).

PLX5622 was acquired from DC Chemicals and incorporated in the cellulose-free and prebiotic diets at a dosage of 1,200 ppm. Mice were switched to the PLX5622 diet at 5-6 weeks of age. Diets were replenished weekly and food intake was measured weekly. Mice were monitored by the lead investigator and Caltech veterinary staff for adverse health effects.

All animal experiments were done under the guidance and approval of Caltech's Institutional Animal Care and Use Committee (IACUC).

Motor Testing

A full battery of motor tests was performed at 22 weeks of age. All motor testing was completed in the same room in a biological safety cabinet between the hours of 6 and 10 of the light phase. Motor testing was completed as described in (Fleming et al. 2004; Sampson et al. 2016). Motor tests were done in the following order: Day 1: beam traversal training, pole training; Day 2: beam traversal training, pole training, wire hang; Day 3: beam traversal test, pole test, hindlimb score, adhesive removal; Day 4: fecal output. Mouse cages were not changed during the duration of testing.

Beam traversal: Time to cross, errors per step, and number of steps were tested using a plexiglass beam 1 m in length. The beam was constructed of four individual segments, with decreasing width of 1 cm increments along the length of the beam (3.5 cm, 2.5 cm, 1.5 cm, and 0.5 cm). Mice were trained for two consecutive days prior to testing on day 3. On each training day, mice were prompted to cross the beam for three consecutive trials. On testing day mice were recorded using a GoPro camera for analysis of errors per step and number of steps.

Pole descent: Time to descend a 24-inch pole wrapped in mesh liner was recorded. The pole was placed in the animal's home cage and mice were trained for two consecutive days prior to testing on day 3. Three trials were performed on day 1 of training: trial 1: mice were gently placed head down on the pole 1/3 of the distance from the base, trial 2: mice were placed head down on the pole 2/3 of the distance from the base, trial 3: mice were placed head down on the top of the pole. On day 2 of training, mice were placed on the top of the pole for three consecutive trials. On testing day, mice were placed on the top of the pole for three trials of testing. The timer was stopped once one of the front hindlimbs touched the base of the pole. Time to descend was averaged across all three trials.

Adhesive removal: A 0.25 in. adhesive, round sticker was placed on the nose of the mouse. The mouse was subsequently placed in its home cage (without cagemates) and time to remove the adhesive was recorded. Time to remove was averaged across two trials.

Wire hang: Mice were placed in the middle of a rectangular wire grid placed over a sterile, clean cage. the wire grid was gently inverted with the mouse hanging over the cage. Time to fall was recorded as the time between grid inversion and the mouse falling off the grid. Maximum time was set to 60 seconds. Time to fall was averaged across two trials.

Hindlimb score: Mice were gently held upwards in the air by the mid-section of their tail and hindlimb movement was observed. Mice were given a score of 0, 1, 2, or 3 depending on the movement and flexibility of their rear hindlimbs. The score was assessed by two experimenters and the average score was reported.

Scores were assigned as follows:

0: rear hindlimbs were flexible and mobile, with a complete range of motion; no inward clasping was observed

1: rear hindlimbs exhibited mild rigidity with hindlimbs orienting inward slightly

2: rear hindlimbs oriented inward, but were not completely clasped

3: rear hindlimbs were firmly clasped together

Microglia Isolation and Sequencing

Microglia isolation: Microglia were isolated from mouse brains at 22 weeks of age. For all experiments, samples were pooled from 4-6 mice/treatment group. Mice were anesthetized and perfused with ice-cold PBS. Brain regions of interest were dissected and homogenized using mechanical dissociation. Single cell suspensions were obtained using a Dounce homogenizer. A 37/70 Percoll density gradient was used to separate cells from debris and myelin. Following Percoll separation, cells were washed and stained with Cd11B (1:1,000, Biolegend), CX3CR1 (1:10,000, Biolegend), CD45 (1:1,000, Biolegend), and DAPI (1:10,000, Sigma-Aldrich). All steps were performed in microglia staining buffer (1X HBSS, 1% BSA and 1 mM EDTA). Cells were sorted in a FACSAria III Fusion flow cytometer (BD Biosciences). Live CD11b+, CX3CR1+, and CD45 (low) cells were identified as microglia and collected for analysis. The full protocol can be found at protocols.io (https://doi.org/10.17504/protocols.io.kqdg3p7bel25/v1)

Single cell sequencing: The v3.1 Chromium Next GEM single cell reagent kit from 10x genomics was used for scRNAseq of FACS-purified microglia. Between 2-4,000 cells were loaded on the Next GEM chip for substantia nigra samples, with 1,000-1,700 cells/group recovered for analysis. For striatum samples, approximately 8-16,000 cells were loaded on the Next GEM chip, with 5-10,000 cells/group recovered for analysis. Library construction was completed according to the manufacturer's instructions. Samples were tagged with a unique sample index, pooled, and sequenced with an average depth of 111k reads/cell on a NovaSeq 6000 sequencing platform (Illumina). Cell Ranger software (10X Genomics) was used for sequence alignment, cluster analysis, and identification of differentially expressed genes between groups. ShinyGO was used for gene ontology and pathway analysis (Ge, Jung, and Yao 2020).

Single-cell transcriptomic analysis: The data were first filtered by removing cells with less than 200 genes and genes that were expressed in less than 100 cells. Gene counts were normalized by dividing the number of times a particular gene appeared in a cell (gene cell count) by the total gene counts in that cell. Counts were multiplied by a constant factor (5,000), a constant value of 1 was added to avoid zeros, and then the data were log transformed. Data analysis steps including Leiden clustering, differential gene expression analysis, and plotting of marker genes were performed using the Scanpy package (Wolf, Angerer, and Theis 2018).

ATAC Seq: FACS-purified microglia were collected as described above and resuspended in 50 µL of ice-cold lysis buffer (10 mM Tris-HCl, pH 7.4, 10 mM NaCl, 3 mM $MgCl_2$, 0.1% IGEPAL CA-630). Cells were spun down at 500 xg for 10 min at 4ºC. Supernatant was discarded and a transposition reaction was performed on the cell pellet using the Illumina Tagment DNA enzyme and buffer kit. Samples were purified using the Zymo ChIP DNA clean and concentrator kit and transposed DNA was eluted in elution buffer. Two independent trials were completed for the experiment.

Immunohistochemistry:

Sectioning: 22-week-old WT and ASO mice were anesthetized with pentobarbital (Euthasol). Mice were perfused with ice-cold phosphate buffered saline (PBS) and 4% paraformaldehyde (PFA). Brains were removed and placed in tissue culture plates with 4% PFA for 48 hours before transfer to PBS+ 0.05% sodium azide. Whole brains were embedded in agarose and sliced coronally into 50 µM sections using a vibratome. Free-floating sections were placed in PBS+ 0.05% sodium azide and stored at 4ºC until staining.

Staining: Sections were permeabilized for 30 minutes in 3% BSA, 0.5% Triton X-100 in PBS, blocked for 1 hour in 3% BSA, 0.1% Triton X-100 in PBS , and stained with IBA-1 (1:1,000, Wako, anti-rabbit) and tyrosine hydroxylase (Th) (1:1,000, Abcam, anti-chicken) overnight at 4ºC (protocol adapted from Datta et al. 2018). Sections were then stained with anti-rabbit IgG AF-647 (1:1,000, Life Technologies) and anti-chicken IgG AF-594 (1:600, Jackson ImmunoResearch). Slices containing brain regions of interest were mounted on a cover slip using

ProLong Diamond anti fade mountant with 4',6-diamidino-2-phenylindole (DAPI). Coverslips were stored at 4ºC until imaging.

Imaging: Images were obtained on a Zeiss LSM800. For diameter measurements: images were taken with a 20X objective, with 3 pictures taken per brain region of interest. Imaris Software was used to measure the diameters of cells, with 30-70 cells counted per brain region/animal. For 3D reconstruction: z-stack images were taken with 1.00 µm steps in the z-direction with a 40X objective. 3D reconstruction was done in the Imaris Software, with 3-6 cells analyzed per brain region/animal.

α-synuclein Aggregation Assays:

Susbtantia nigra and striatum were dissected on ice from 22-week-old mice and stored at -80ºC until used.

Protein extraction: Brain tissues were lysed using Tissue Extraction Reagent (ThermoFisher) and protease inhibitor. Samples were homogenized for 90 seconds using a bead beater and were placed directly on ice for 10-15 minutes following homogenization. Lysates were centrifuged at 10k rpm for 5 minutes and supernatants were collected and stored at -80ºC for later use. The full protocol can be found at protocols.io (https://doi.org/10.17504/protocols.io.5jyl896o6v2w/v1)

α -synuclein aggregation: Levels of aggregated α-synuclein were determined using the dot blot assay. Samples were quantified using the Pierce BCA Protein assay kit (Thermo Fisher) and normalized to equal concentrations between 0.5-1.0 ng/µL in water. 1 µg of sample was spotted on dry nitrocellulose membrane (0.45 µm). Samples were blocked in 5% skim milk in Tris-buffered saline with 0.1% Tween-20 (TBS-T) and stained with anti-aggregated α-synuclein antibody (1:1,000, Abcam) overnight at 4ºC. The next day, blots were stained with anti-rabbit IgG-HRP (1:1,000, Cell Signaling) for 2 hours. Signal was detected using Clarity chemiluminescence substrate (Bio-Rad) and imaged on a Bio-Rad digital imager. Integrated density is reported as the intensity of an identically-sized area of each dot for each sample. The full protocol can be found at protocols.io (https://doi.org/10.17504/protocols.io.261gen2xdg47/v1)

RNA Extraction and qPCR:

Brain regions were dissected on ice from 22-week-old mice and stored at -80ºC in RNAlater solution (Thermo Fisher) until RNA extraction.

RNA extraction: RNA was extracted using either Direct-zol RNA Microprep or Miniprep kit (Zymo Research) depending on the size of the brain region.

qPCR: RNA was transcribed using the iScript ™ cDNA synthesis kit (Bio-Rad) per the manufacturer's instructions. SYBR Green master mix was used for qPCR reactions. Primers used for experiments were: HDAC1: 5'-GAACTGCTAAAGTACCACC-3' & 5'-CATGACCCGGTCTGTAGTAT-3; HDAC2: 5'-CGGTGTTTGATGGACTCTTTG-3' & 5'-CCTGATGCTTCTGACTTCTTG-3'; HDAC6: 5'-CTGCATGGCATCGCTGGTA-3' & 5'-GCATCAAAGCCAGTGAGATC-3' ; HDAC7: 5'-CTCGGCTGAGGACCTAGAGA-3' & 5'-CAGAGAAATGGAGCCTCTGC-3' ; HDAC9: 5'-GCGGTCCAGGTTAAAACAGAA-3' & 5'-GCCACCTCAAACACTCGCTT-3' ; GAPDH: 5'-CATGGCCTTCCGTGTTCCTA-3' & 5'-CCTGCTTCACCACCTTCTTGAT-3'; FFAR2: 5'-TTCCCATGGCAGTCACCATC-3' & 5'-TGTAGGGTCCAAAGCACACC-3'; FFAR3: 5'-ACCGCCGTCAGGAAGAGGGAG-3' & 5'TCCTGCCGTTTCGCSTGGTGG-3'

Isolation of Immune Cells from Intestinal Lamina Propria/Spleen and Flow Cytometry:

For isolation of intestinal lamina propria cells, the small and large intestines were dissected and placed immediately into ice-cold PBS. After mesenteric fat and Peyer's patches (small intestine) were removed, the intestines were longitudinally opened and luminal contents were washed out with cold PBS. Tissue pieces were washed for 10 min in 1 mM dithiothreitol (DTT)/PBS at room temperature on a rocker to remove mucus, followed by a wash for 25 min in 10 mM EDTA/30 mM HEPES/PBS at 37ºC on a platform shaker (180 rpm) to remove epithelium. After a 2 min wash in complete RPMI, tissue was digested in a 6-well plate for 1.5hrs in complete RPMI with 150 U/mL (small intestine) or 300 U/mL (large intestine) collagenase VIII (Sigma-Aldrich) and 150 µg/mL DNase (Sigma-Aldrich) in a cell culture incubator (5% CO_2). Tissue digests were passed through a 100 µm cell strainer and separated by centrifugation (1,200 xg for 20 min) using a 40/80% Percoll gradient. Immune cells were collected at the 40/80% interface. For the

spleen, the tissue was passed through a 100 μm cell strainer and incubated in red cell lysis buffer (Sigma-Aldrich) for 8 min at room temperature. Both spleen and intestine immune cells were washed with 0.5% BSA/PBS before staining and fixation (eBioscience Foxp3 / Transcription Factor Staining Buffer Set).

For flow cytometry staining, CD16/32 antibody (eBioscience) was used to block non-specific binding to Fc receptors before surface staining. Immune cells were stained with antibodies against the following markers: CD103 (PerCP-efluor710), CD11b (SuperBright645), CD11c (FITC), CD19 (FITC), CD3e (PE), CD4 (APC), CD45.2 (BV421), CD64 (APC-Cy7), CD8a (APC-e780), CSF1R (PE), Ly6C (APC), MHCII I-A/I-E (PE or PerCP-efluor710), TCRβ (PerCP-Cy5.5). For some panels, a lineage marker mix (Lin) contained TCRβ, B220, Ly6G and Siglec-F (PE-Cy7). Live and dead cells were discriminated by Live/Dead Fixable Aqua Dead Cell Stain Kit (Invitrogen).

Gut Microbiome Profiling:

Metagenomic Sequencing: Shotgun sequencing libraries were generated using the Kapa HyperPlus protocol on gDNA extracted from mouse fecal pellets. Samples were sequenced using 150 bp paired end reads on an Illumina NovaSeq 6000 at the UCSD IGM Genomics Center.

Metagenomic Analyses: Quality control filtering and read alignment of metagenomic reads was conducted with Qiita (study-id 13244). First, adapter removal and quality trimming were conducted using Atropos v1.1.24. To generate taxonomic and functional gene-level profiles we applied the Woltka v0.1.1 pipeline to align reads against the Web of Life database (Zhu et al. 2019) using Bowtie2 v2.3.0 (Langmead and Salzberg 2012), followed by generation of Operational Genomic Units (Zhu et al. 2021). Downstream statistical analyses and data visualization was conducted in R (v4.1.0). For community-level measures, including alpha- and beta-diversity, Woltka-generated taxonomic predictions at the species level were rarefied to an even depth of 321,980 counts. Alpha-diversity metrics including Observed Species, Simpson's Evenness, and Gini's Dominance were calculated using the microbiome R package and tested for statistical significance using a one-way ANOVA for treatment group and post-hoc Tukey's test for pairwise comparisons. Assessment of between-sample diversity was accomplished using the

Bray-Curtis distance. We estimated metadata-explained variance using the Bray-Curtis distance with permutational multivariate analysis of variance (PERMANOVA) with 9,999 permutations followed by multiple hypothesis testing corrections using the Benjamini-Hochberg method (FDR = 0.1). Differential abundance testing was conducted using Multivariable Association with Linear Models (MaAsLin2)(Mallick et al. 2021). For data preparation, we applied a 10% prevalence filter, total sum scale normalization, and an arcsine square root transformation for variance stability. We then applied a feature-level-specific variance filter based on the variance distribution and the number of features present at each level. MaAsLin2 linear models were fit with genotype and diet variables as fixed effects.

SCFA fecal measurements (LC-MS): Fecal samples were collected from mice at 22 weeks of age and stored at -80 ^{o}C until analysis. Sample preparation: Mouse fecal samples were extracted and derivatized as described previously (Chan et al. 2017). Briefly, ice-cold extraction solvent (1:1 v/v acetonitrile/water) was added to fecal sample at a ratio of 2 µL:1 mg sample and internal standard mix to a final concentration of 100 µM. The suspension vortex mixed for 3 min at room temperature, sonicated for 15 min, and then centrifuged at 18,000 x g for 15 min at 4 ^{o}C. An aliquot of 100 µL was subsequently derivatized using a final concentration of 10 mM aniline and 5 mM 1-ethyl-3-(3-dimethylaminopropyl)carbodiimide hydrochloride (EDC) (ThermoFisher) for 2 h at 4 ^{o}C. The derivatization reaction was quenched using a final concentration of 18 mM succinic acid and 4.6 mM 2-mercaptoethanol for 2 h at 4 ^{o}C. All samples were stored at 4 ^{o}C until analysis on the same day. Mixed calibrators of acetic acid, propanoic acid, butyric acid and isobutyric acid (10nM - 10×10^{3} nM) (Sigma-Aldrich) together with single- and double- blanks, spiked with internal standard mix (Acetic acid-d3, propanoic acid-d2, butyric acid-d2) (Pointe-Claire) to a final concentration of 100 µM were prepared and subjected to the same sample preparation procedure as fecal samples. The full protocol can be found at protocols.io (https://doi.org/10.17504/protocols.io.bp2l61rrkvqe/v1)

Liquid Chromatography Mass Spectrometry (LC-MS): Derivatized samples were analyzed using an ultra-high-performance liquid chromatography (UHPLC) system 1290 connected to a quadrupole time of flight (Q-TOF 6545) mass spectrometer (Agilent Technologies) equipped with an orthogonal DUAL AJS-ESI interface. Samples were subjected to reverse phase C18

separation (Phenomenex Scherzo SS-C18 100 x 2 mm) and data were collected in positive ion mode. Data were acquired from 50 to 750 m/z-1 at 2 spectra s^{-1}. Electrospray ionization (ESI) source conditions were set as follows: gas temperature 325 °C, drying gas 9 L min^{-1}, nebulizer 35 psi, fragmentor 125 V, sheath gas temperature 350 °C, sheath gas flow 8 L min^{-1}, nozzle voltage 1000 V. For reverse phase C18 chromatographic separation, a two-solvent gradient running at 0.3 mL min^{-1} (Mobile Phase: A: 100:0.1 Water:Formic Acid, B: 100:0.1 Isopropanol:Formic Acid) was used. the column was equilibrated at 15% B for 1 min and a sample was introduced. The solvent ratio was then increased from 15% B to 100% B over 13 min and then reduced back to 15% B over 2 min. Injection volume was 5 µL with a column temperature of 45° C. The LC-MS/MS data acquired using Agilent Mass Hunter Workstation (.d files) were processed in quantitative analysis software (Agilent Technologies) for quantitative analysis of samples. The linear calibration plots for acetic acid, propanoic acid, butyric acid and isobutyric acid were constructed using peak area ratios of each analyte to the IS versus the concentrations of calibrators (x) with 1/x weighting, and the least squares linear regression equations were obtained as the calibration equations for individual analytes.

SCFA brain measurements (UHP-LC): Striatum and substantia nigra were dissected from 22-week-old mice, placed in dry ice, and stored at -80ºC until analysis. Samples were analyzed by BIOTOOLS CO. using an ultra-high-performance liquid chromatography (UHPLC) system. Brain tissue samples were extracted with 70% methanol for 30 mins, using a sample:solvent ratio of 1 mg:40 µL. The sample was centrifuged at 21,380 rcf for 5 min at 4°C. The supernatant was used for derivatization procedures. Each sample was mixed with 5 µL of 0.1 mM internal standard and 200 µL each of pyridine, 1-EDC-HCl, and 2-NPH-HCl solutions as reaction-assistive agents, and reacted at 45°C for 20 min. 100 µL of potassium hydroxide solution was added (to stop the reaction) and reacted at 45°C for 15 min. After cooling, the mixture was ultrasonicated with 1 mL of phosphoric acid aqueous solution and 2 mL of ether for 3 min and then centrifuged for 5 min at 2,054 rcf. The ether layer was collected and spun-dry. The sample was reconstituted with 25 µl MeOH. Mass analysis: Each sample (2 µL) was injected into a vanquish ultra-high-performance liquid chromatography (UHPLC) system coupled with SCIEX QTrap® 5500. UHPLC parameters were set as follows: A CSH 1.7 µm, 2.1x100 mm column (Waters) was used. The column oven temperature was set at 45°C. The binary mobile phase

included deionized water containing 5 mM ammonium acetate as solvent A, and acetonitrile with 5 mM ammonium acetate as solvent B. The flow rate was 0.35 mL/min with a linear gradient elution over 15 min. Reagent 1: Pyridine (Sigma-Aldrich) was adjusted with methanol to 3% (V/V) (Weng et al. 2020).

Statistical Analysis:

Graphpad Prism software (version 9.0) was used for statistical analysis. Data presented represent mean ± SEM, with each data point representing values from an individual mouse. All behavioral and molecular data were analyzed by two-way ANOVA followed by Tukey's multiple comparisons test, unless stated otherwise. *p<0.05, **p<0.01, ***p<0.001, and ****p<0.0001

Data Availability

All datasets generated or analyzed in this study can be found through the Zenodo depository: https://doi.org/10.5281/zenodo.6377704 All experimental protocols can be found on protocols.io.

List of reagents

Reagent type (species) or resource	Designation	Source of reference	Identifier	Additional information
Mus musculus	Thy1-α-synuclein (line 61)	(Chesselet et al. 2012; Rockenstein et al. 2002)	ASO	
Antibody	Anti-beta actin, rabbit polyclonal	Abcam	Ab8227	1:1,000
Antibody	Anti-aggregated α-synuclein, rabbit polyclonal	Abcam	Ab209538	1:1,000
Antibody	Anti-Iba1, rabbit polyclonal	Wako	019–19741	1:1,000
Antibody	Anti-tyrosine hydroxylase, chicken polyclonal	Abcam	ab76442	1:1,000
Antibody	Anti-rabbit IgG-647, donkey polyclonal	Life Technologies	1874788	1:1,000
Antibody	Anti-chicken IgG-594, donkey polyclonal	Jackson Immunoresearch	703-585-155	1:600
Antibody	Anti-rabbit IgG, HRP-linked	Cell Signaling	7074	1:1,000

Antibody	Anti-mouse/human CD11b-APC, rat monoclonal	BioLegend	101211	1:1,000
Antibody	Anti-mouse CX3CR1-PE/Cyanine7, mouse monoclonal	BioLegend	149016	1:10,000
Antibody	Anti-mouse CD45-Alexa Flour 488, rat monoclonal	BioLegend	103121	1:1,000
Antibody	DAPI	Sigma-Aldrich	10236276001	1:10,000
Antibody	Aqua Viability Dye	ThermoFisher/Invitrogen	L34957	1:1,000
Antibody	CD16/CD32 Monoclonal Antibody (93), eBioscience™ (1mg)	ThermoFisher	14-0161-86	1:100
Antibody	CD3e Monoclonal Antibody (145-2C11), PE, eBioscience™	ThermoFisher	12-0031-82	1:200
Antibody	CD4 Monoclonal Antibody (GK1.5), APC, eBioscience™	ThermoFisher	17-0041-83	1:200
Antibody	TCR beta Monoclonal Antibody (H57-597), PerCP-Cyanine5.5, eBioscience™	ThermoFisher	45-5961-82	1:200
Antibody	CD8a Monoclonal Antibody (53-6.7), APC-eFluor 780, eBioscience™	ThermoFisher	47-0081-82	1:200
Antibody	CD11c Monoclonal Antibody (N418), FITC, eBioscience™	ThermoFisher	11-0114-82	1:200
Antibody	CD170 (Siglec F) Monoclonal Antibody (1RNM44N), PE-Cyanine7, eBioscience™	ThermoFisher	25-1702-82	1:200
Antibody	Ly-6C Monoclonal Antibody (HK1.4), APC, eBioscience™	ThermoFisher	17-5932-82	1:200
Antibody	CD103 (Integrin alpha E) Monoclonal Antibody (2E7), PerCP-eFluor 710, eBioscience	ThermoFisher	46-1031-82	1:200
Antibody	CD64 Monoclonal Antibody (X54-5/7.1), APC-eFluor 780, eBioscience™	ThermoFisher	47-0641-82	1:200
Antibody	CD11b Monoclonal Antibody (M1/70), Super Bright 645, eBioscience™	BioLegend	64-0112-82	1:200
Antibody	BV421 anti-mouse CD45.2	Tonbo	109831	1:200
Antibody	PE-Cy7 anti-mouse Ly6G	Tonbo	60-1276-U100	1:200
Antibody	PE-Cy7 anti-mouse TCRb	Tonbo	60-5961-U100	1:200
Antibody	PE-Cy7 anti-mouse B220	Tonbo	60-0452-U100	1:200
Antibody	FITC anti-mouse CD19	Tonbo	35-0193-U500	1:200
Antibody	PE Anti-Mouse MHC Class II (I-A/I-E) (M5/114.15.2)	Tonbo	50-5321-U100	1:200

Antibody	PE anti-mouse CD115 (CSF-1R) Antibody	BioLegend	135506	1:200
Antibody	MHC Class II (I-A/I-E) Monoclonal Antibody (M5/114.15.2), PerCP-eFluor 710, eBioscience™	ThermoFisher	46-5321-82	1:200
Reagent	eBioscience™ Foxp3 / Transcription Factor Staining Buffer Set	ThermoFisher	00-5523-00	
Reagent	PLX5622	DC Chemicals	DC21518	
Reagent	IL-6 Mouse ELISA kit	ThermoFisher	88-7064-88	
Reagent	TNF-α Mouse ELISA Kit	ThermoFisher	88-7324-77	
Reagent	Tagment DNA enzyme and buffer kit	Illumina	20034197	
Reagent	Prolong Diamond antifade mountant with DAPI	Invitrogen	P36971	
Reagent	Tissue Extraction Reagent I	ThermoFisher	FNN0071	
Reagent	Chromium Next GEM Single Cell 3' GEM, Library & Gel Bead Kit v3.1	10x Genomics	1000128	
Reagent	Chromium Next GEM Chip G Single Cell Kit	10x Genomics	1000127	
Reagent	Single Index Kit T Set A	10x Genomics	2000240	
Reagent	ChiP DNA clean and concentrator	Zymo	D5205	
Reagent	Direct-zol RNA Microprep	Zymo	R2062	
Reagent	Direct-zol RNA Miniprep	Zymo	R2050	
Reagent	iScript ™ cDNA synthesis kit	Bio-Rad	1708890	
Reagent	Clarity ™ Western ECL Substrate	Bio-Rad	1705060	
Sequence-based reagent	HDAC1: 5'-GAACTGCTAAAGTACCACC-3' 5'-CATGACCCGGTCTGTAGTAT-3'			
Sequence-based reagent	HDAC2: 5'-CGGTGTTTGATGGACTCTTTG-3' 5'-CCTGATGCTTCTGACTTCTTG-3'			
Sequence-based reagent	HDAC6: 5'-CTGCATGGCATCGCTGGTA-3' 5'-GCATCAAAGCCAGTGAGATC-3'			

Sequence-based reagent	HDAC7: 5'-CTCGGCTGAGGACCTAGAGA-3' 5'-CAGAGAAATGGAGCCTCTGC-3'			
Sequence-based reagent	HDAC9: 5'-GCGGTCCAGGTTAAAACAGAA-3' 5'-GCCACCTCAAACACTCGCTT-3'			
Sequence-based reagent	GAPDH: 5'-CATGGCCTTCCGTGTTCCTA-3' 5'-CCTGCTTCACCACCTTCTTGAT-3'			
Sequence-based reagent	FFAR2: 5'-TTCCCATGGCAGTCACCATC-3' 5'-TGTAGGGTCCAAAGCACACC-3'			
Sequence-based reagent	FFAR3: 5'-ACCGCCGTCAGGAAGAGGGAG-3' 5'TCCTGCCGTTTCGCSTGGTGG-3'			

831

Acknowledgements

We thank members of the Mazmanian laboratory and Dr. Catherine Oikonomou for critical review of this manuscript. We thank the Caltech Office of Laboratory Animal Research (OLAR) for animal husbandry, Dr. Wei-Li Wu for assistance with SCFA brain measurements, Dr. Sisi Chen and the Caltech Single-Cell Profiling and Engineering Center (SPEC) for technical assistance and support, the Caltech Flow Cytometry and Cell Sorting Facility for technical assistance, the Caltech Bioinformatics Center for data analysis support, and the Caltech Biological Imaging Facility (BIF) for training and use of confocal microscopes. We thank Prof. Chen-Chih Hsu's laboratory in the Department of Chemistry at National Taiwan University and BIOTOOLS Co., Ltd. for the feces and brain SCFA measurements. R.A. was supported by the U.S. Department of Defense, the Donna and Benjamin M. Rosen Bioengineering Center, and the Biotechnology Leadership Program at Caltech. This study was funded by grants to S.K.M. from the U.S. Department of Defense (PD160030), Heritage Medical Research Institute (HMRI-15-09-01), and by the joint efforts of the Michael J. Fox Foundation for Parkinson's Research (MJFF) and the Aligning Science Across Parkinson's (ASAP) initiative. MJFF administers the grant (ASAP-000375) on behalf of ASAP and itself.

Competing Interests

A.K., T.C-J., and B.R.H. have equity in RiteCarbs, a company developing prebiotic diets for Parkinson's disease. S.K.M. has equity in Axial Therapeutics, a company developing gut-restricted drugs for Parkinson's disease.

Figure 1

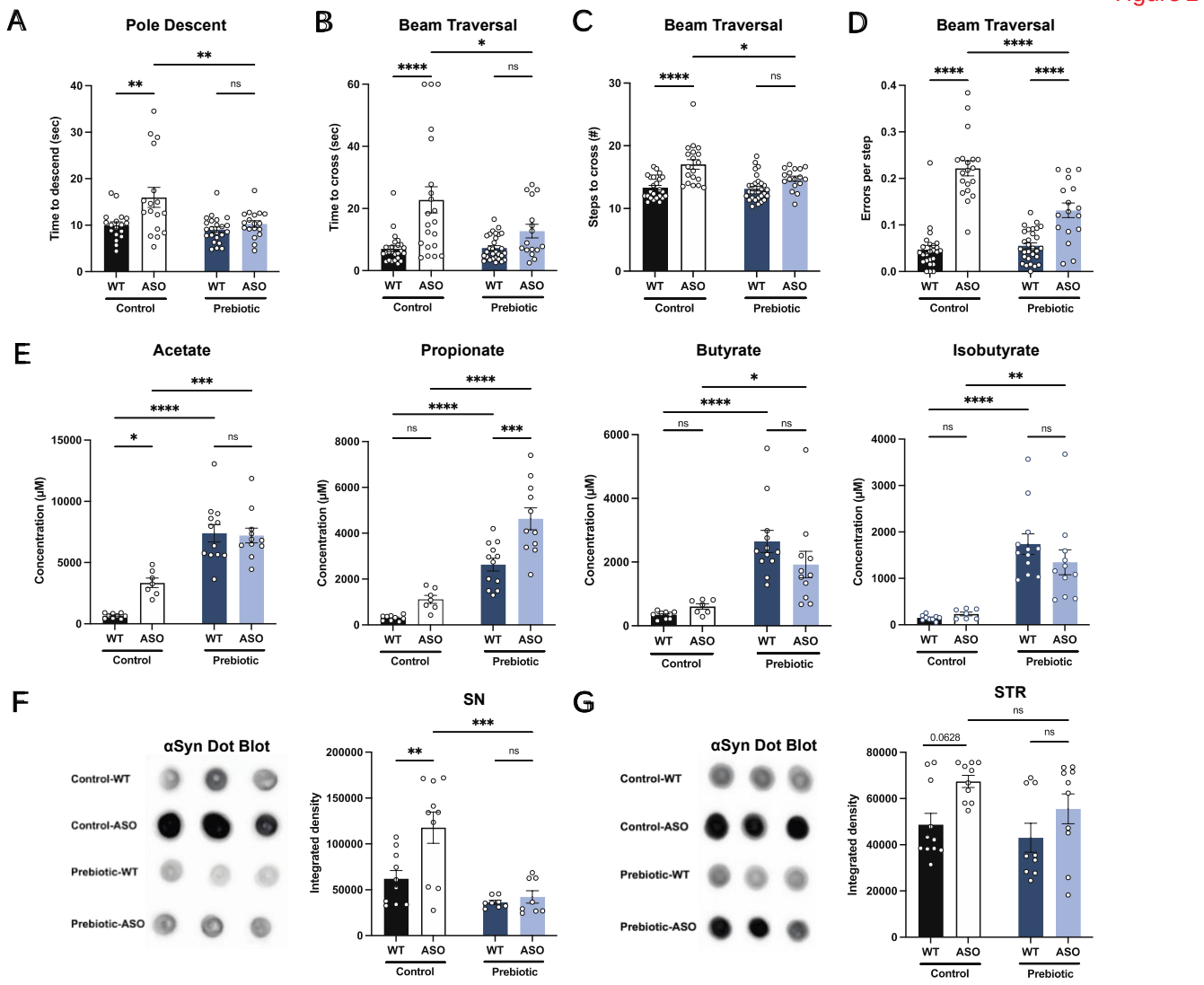

Figure 1. Prebiotic diet attenuates motor symptoms and reduces αSyn aggregation
A-D) Motor behavior metrics at 22 weeks of age for prebiotic- and control-fed WT and ASO mice from pole descent (B) and beam traversal (C-E) tests. Motor test data is derived from two independent experiments (n=16-29/group). **E)** Concentrations (μM) of acetate, propionate, butyrate, and isobutyrate in fecal samples collected from prebiotic-fed WT and ASO mice (n=7-12/group). **F-G)** Aggregated α-synuclein levels in the substantia nigra (SN) (F; n=8-10/group) and striatum (STR) (G; n=9-11/group) measured by dot blot. Each point represents data from one mouse. Data analyzed by two-way ANOVA followed by Tukey's multiple comparisons test. Bars represent mean ± SEM. *p<0.05, **p<0.01, ***p<0.001, and ****p<0.0001.

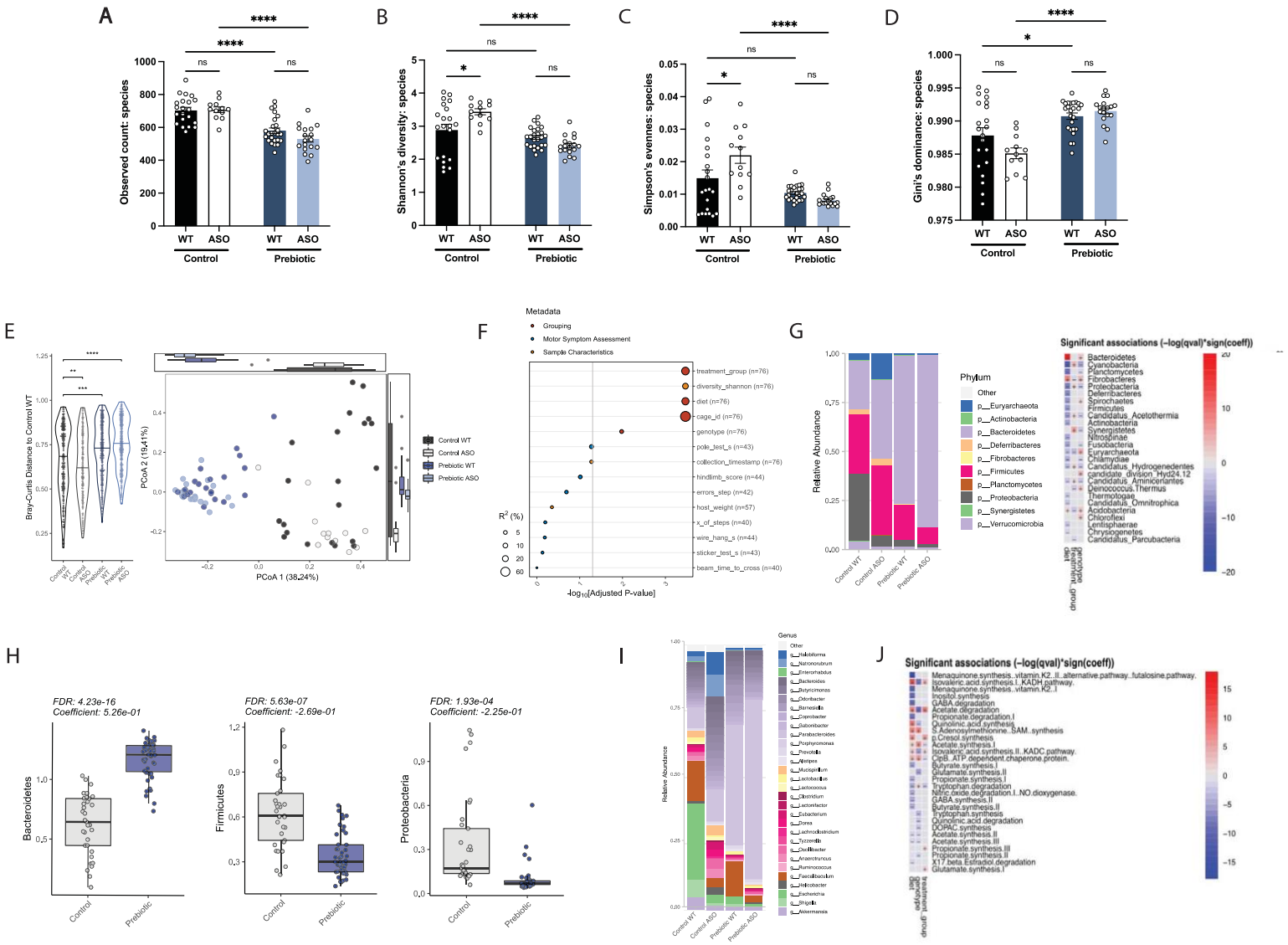

Figure 2. Prebiotic diet alters gut microbiome composition

A-D) Diversity metrics from metagenomic analysis of treatment groups at 22 weeks of age, including observed species count (A), Shannon's diversity (B), Simpson's evenness (C), and Gini's dominance (D). **E)** Principal Coordinate Analysis (PCoA) plot of Bray-Curtis dissimilarity (n=12-25/group). **F)** PERMANOVA analysis summary of Bray-Curtis dissimilarity. **G)** Relative abundance of phyla among treatment groups (left) and heat map showing differentially abundant phyla (right). Diet values are displayed relative to control diet and genotype values relative to WT mice. **H)** Relative abundance of select phyla in treatment groups. **I)** Summary plot of relative abundance of genera. **J)** Differentially expressed pathways identified from the "Gut Microbiome-Brain module". Diet values are displayed relative to control diet and genotype values relative to WT mice (n=12-25/group).

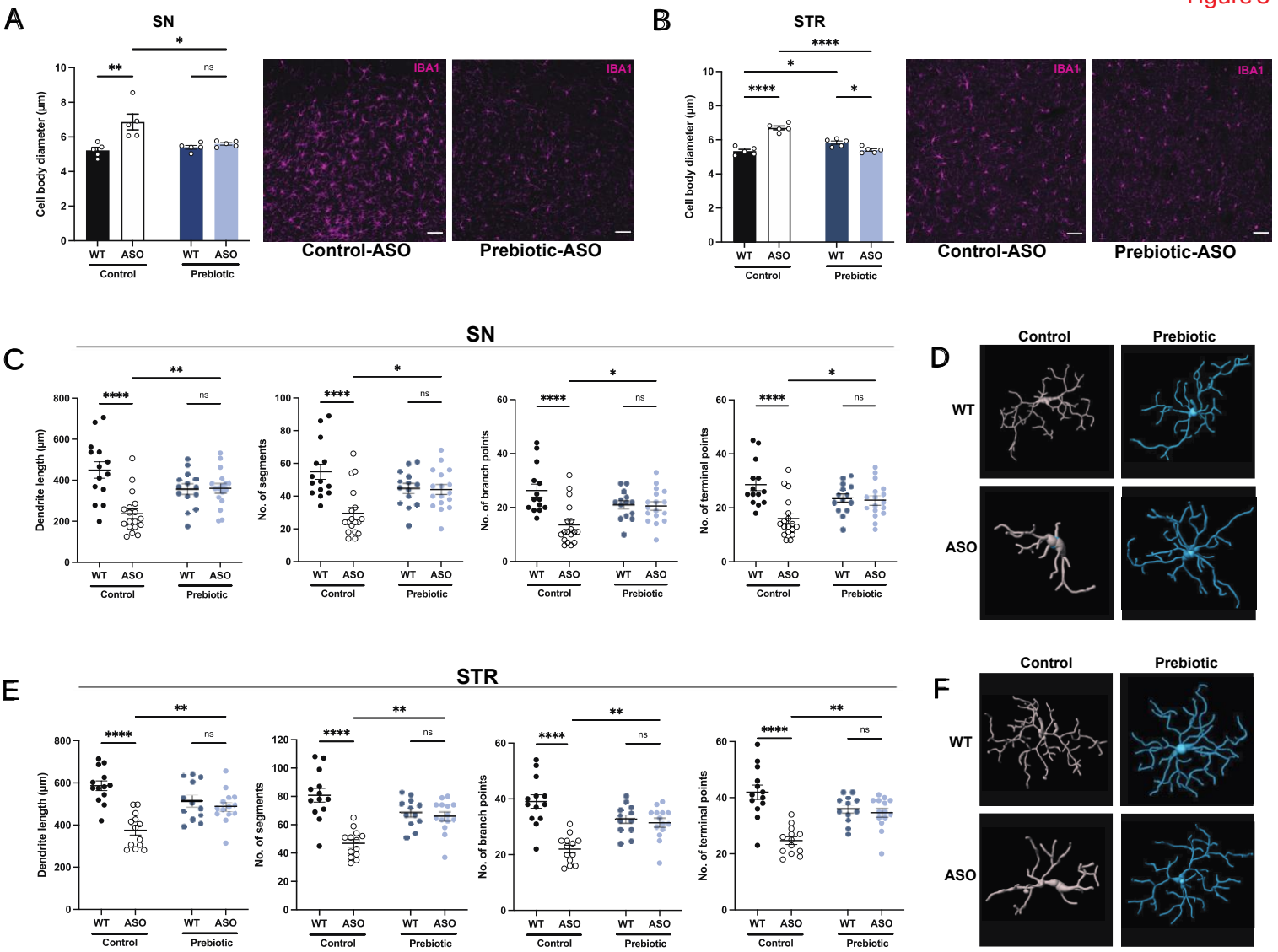

873 **Figure 3. Prebiotic diet alters microglia morphology and reactivity status in ASO mice**
874 **A,B)** Measurement of IBA1+ microglia diameter in substantia nigra (SN) (A; n=5/group) and
875 striatum (STR) (B; n=5/group). Left: quantification of cell diameter. Each point represents one
876 mouse with 26-79 cells measured per mouse. Right: Representative 20x images of IBA1+
877 staining. Scale bars 50 µm. **C-F)** 3D reconstruction of microglia in the substantia nigra (C-D)
878 and striatum (E-F). C,E) Quantification of dendrite length, number of segments, number of
879 branch points, and number of terminal points (n=14-18/group for SN and n=12-14/group for
880 STR). Each point represents one cell, with 3-5 cells analyzed/mouse. D,F) representative 3D
881 reconstructions of microglia imaged at 40x magnification. Data analyzed by two-way ANOVA
882 followed by Tukey's multiple comparisons test. Bars represent mean ± SEM. *p<0.05,
883 **p<0.01, ***p<0.001, and ****p<0.0001.

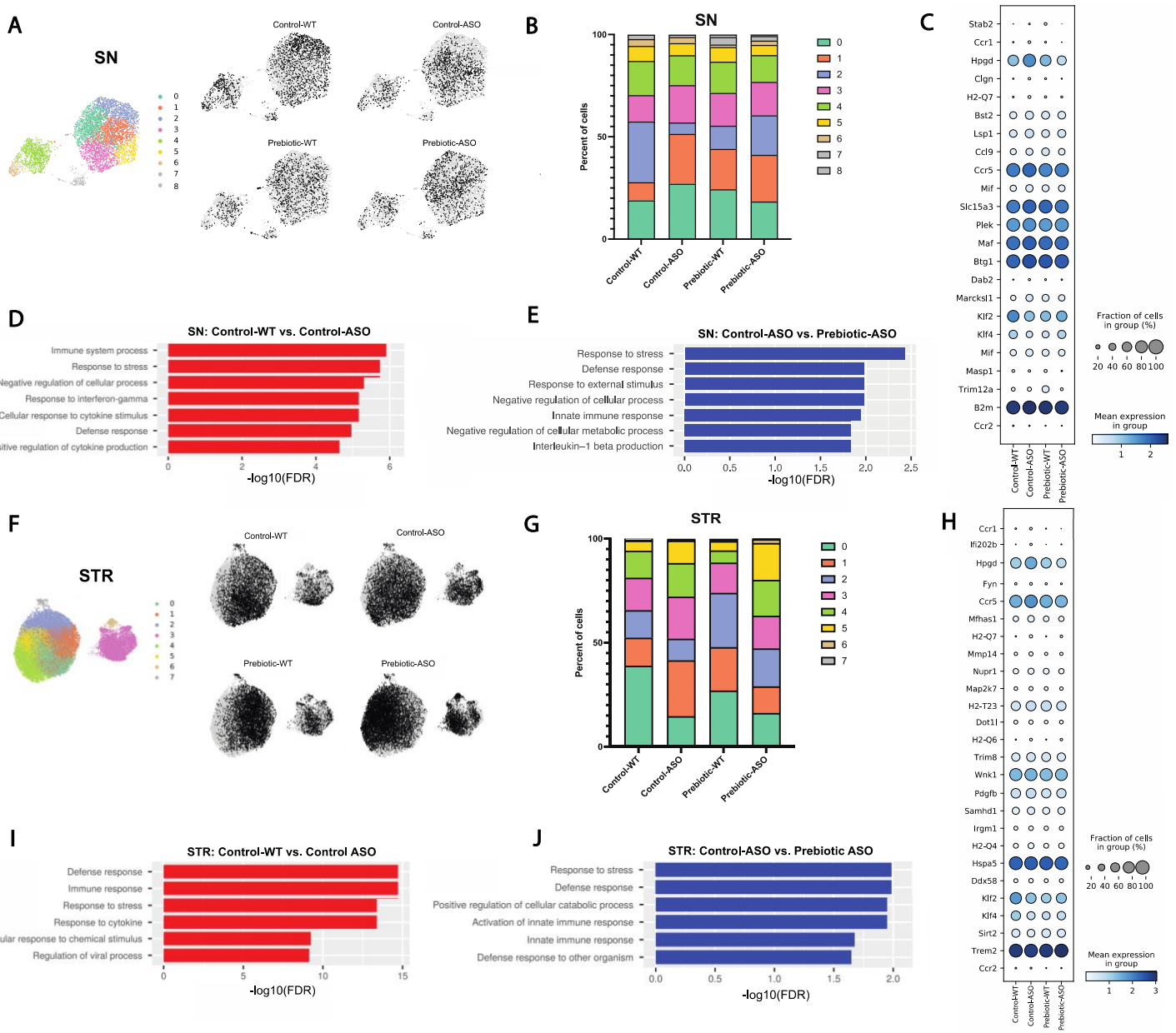

884 **Figure 4. Prebiotic diet alters microglial gene expression**
885 **A)** UMAP plot of all 5,278 substantia nigra (SN) cells sequenced by scRNA-seq from all four
886 treatment groups (left) and distribution of cells from individual samples (right). **B)** Relative
887 distribution of cells within each cluster in the SN. **C)** Dot plot showing genes significantly
888 upregulated in control-ASO microglia (relative to control-WT) and significantly downregulated
889 in prebiotic-ASO microglia (relative to control-ASO) in the SN. **D)** Significantly enriched
890 pathways among 163 genes upregulated in control-ASO microglia relative to control-WT
891 microglia in the SN. **E)** Significantly enriched pathways among 156 genes downregulated in
892 prebiotic-ASO microglia relative to control-ASO microglia in the SN. **F)** UMAP plot of all
893 27,152 striatal (STR) cells sequenced by scRNA-seq from all four treatment groups (left) and
894 distribution of cells from individual samples (right). **G)** Relative distribution of cells within each
895 cluster in the STR. **H)** Dot plot and showing genes significantly upregulated in control-ASO
896 microglia (relative to control-WT) and significantly downregulated in prebiotic-ASO microglia

(relative to control-ASO) in the STR. **I)** Significantly enriched pathways among the 50 most upregulated genes in control-ASO microglia relative to control-WT microglia in the STR. **J)** Significantly enriched pathways among the 50 most downregulated genes in prebiotic-ASO microglia relative to control-ASO microglia in the STR.

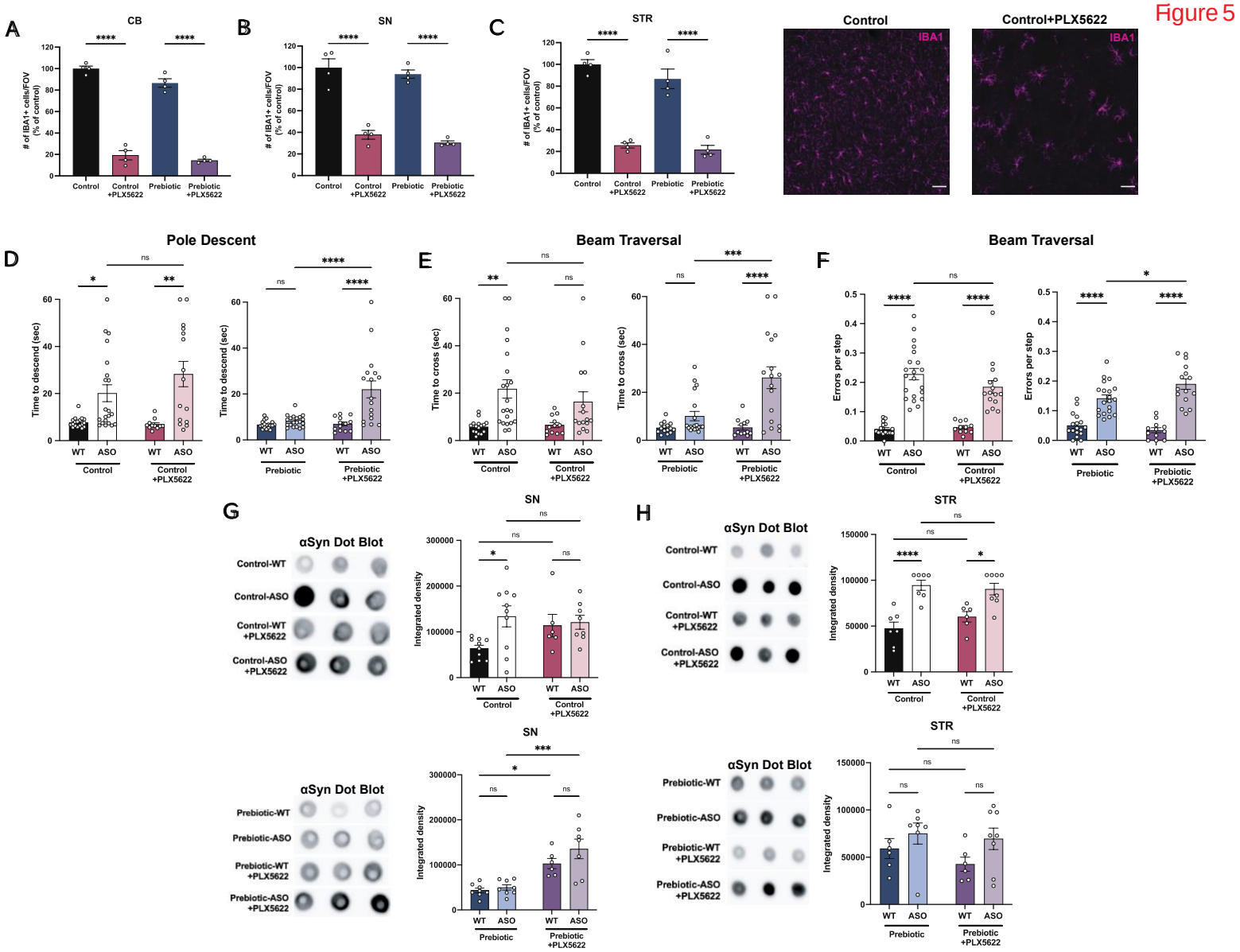

Figure 5. Depletion of microglia inhibits beneficial effects of prebiotics

A-C) Number of IBA1+ cells per field of view in 20X images of the cerebellum (A), substantia nigra (B), and striatum (C). n=4/group. Representative images from the striatum are shown at right (scale bars: 50 μm). **D-F)** Motor performance metrics for pole descent (D) and beam traversal (E-F) tests. Motor data derived from five independent cohorts (n=12-21/group). **G,H)** Aggregated α-synuclein measured by dot blot in the substantia nigra (G; n=6-10/group) and striatum (H; n=6-8/group). Microglia count data analyzed by one-way ANOVA followed by Tukey's multiple comparisons test. Motor and αSyn data analyzed by two-way ANOVA followed by Tukey's multiple comparisons test. Data represent mean ± SEM. *p<0.05, **p<0.01, ***p<0.001, and ****p<0.0001.

Supplement 1

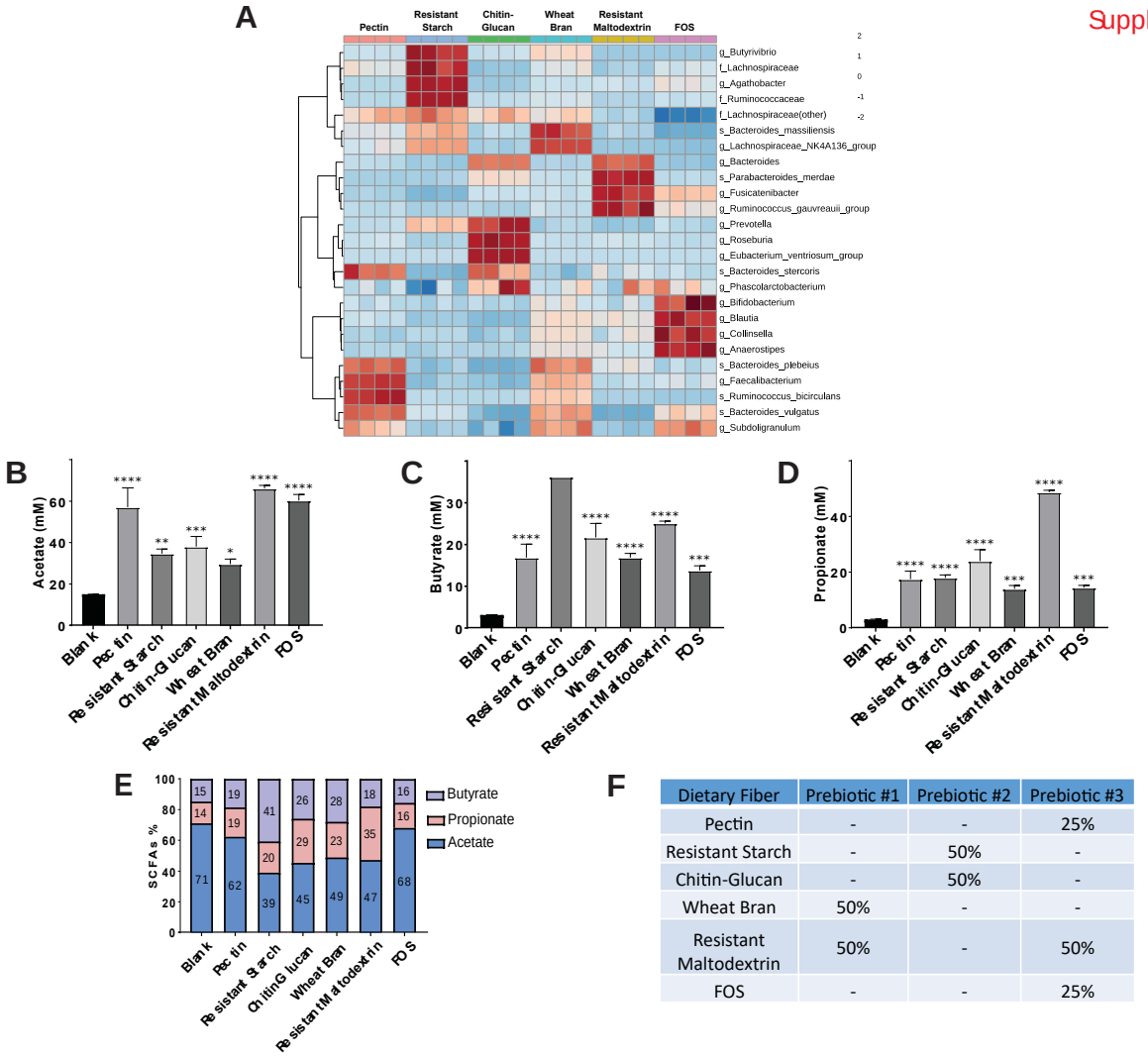

F

Dietary Fiber	Prebiotic #1	Prebiotic #2	Prebiotic #3
Pectin	-	-	25%
Resistant Starch	-	50%	-
Chitin-Glucan	-	50%	-
Wheat Bran	50%	-	-
Resistant Maltodextrin	50%	-	50%
FOS	-	-	25%

Supplement Figure 1. Effect of dietary fibers on gut microbial community and metabolic function *in vitro*

A) Hierarchical clustering of the 25 most abundant genera after 24 h of *in vitro* fecal fermentation using a pooled human gut microbiota community, as previously described (Cantu-Jungles et al. 2018). Taxa were associated with fiber type by hierarchical clustering using Euclidean distances and the Ward algorithm. **B-D)** SCFA concentration (mM) in fecal slurries of acetate (B), butyrate (C) and propionate (D). Data analyzed by two-way ANOVA followed by Tukey's multiple comparisons test. Statistical differences from the blank are indicated by *p<0.05, **p<0.01, ***p<0.001, and ****p<0.0001. **E)** Relative proportion of each SCFA produced in the 24 h *in vitro* fecal fermentation, showing association with fiber type. **F)** Fiber composition of Prebiotic Diets 1-3.

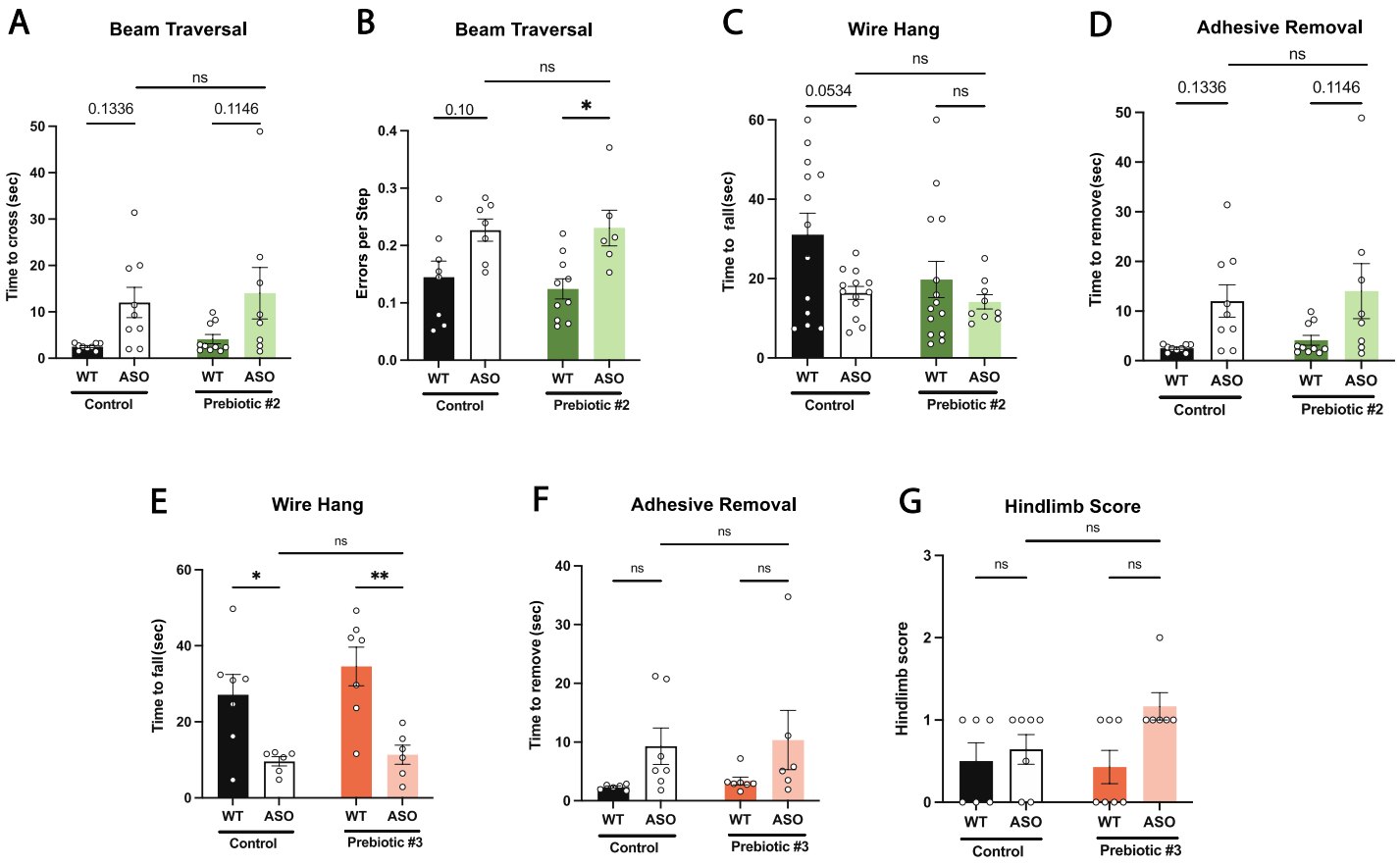

Supplement Figure 2. Motor behavior in mice fed Prebiotic #2 and Prebiotic #3 diets **A-D)** Motor behavior metrics for mice fed Prebiotic #2 diet from beam traversal (A,B), wire hang (C), and adhesive removal (D) tests. **E-G)** Motor behavior metrics for mice fed Prebiotic #3 diet from wire hang (E), adhesive removal (F), and hindlimb score (G) tests (n=6-7/group). Data analyzed by two-way ANOVA followed by Tukey's multiple comparisons test, except for hindlimb score data, which was analyzed by Kruskal-Wallis test. Bars represent mean ± SEM. *p<0.05, **p<0.01, ***p<0.001, and ****p<0.0001.

Supplement 3

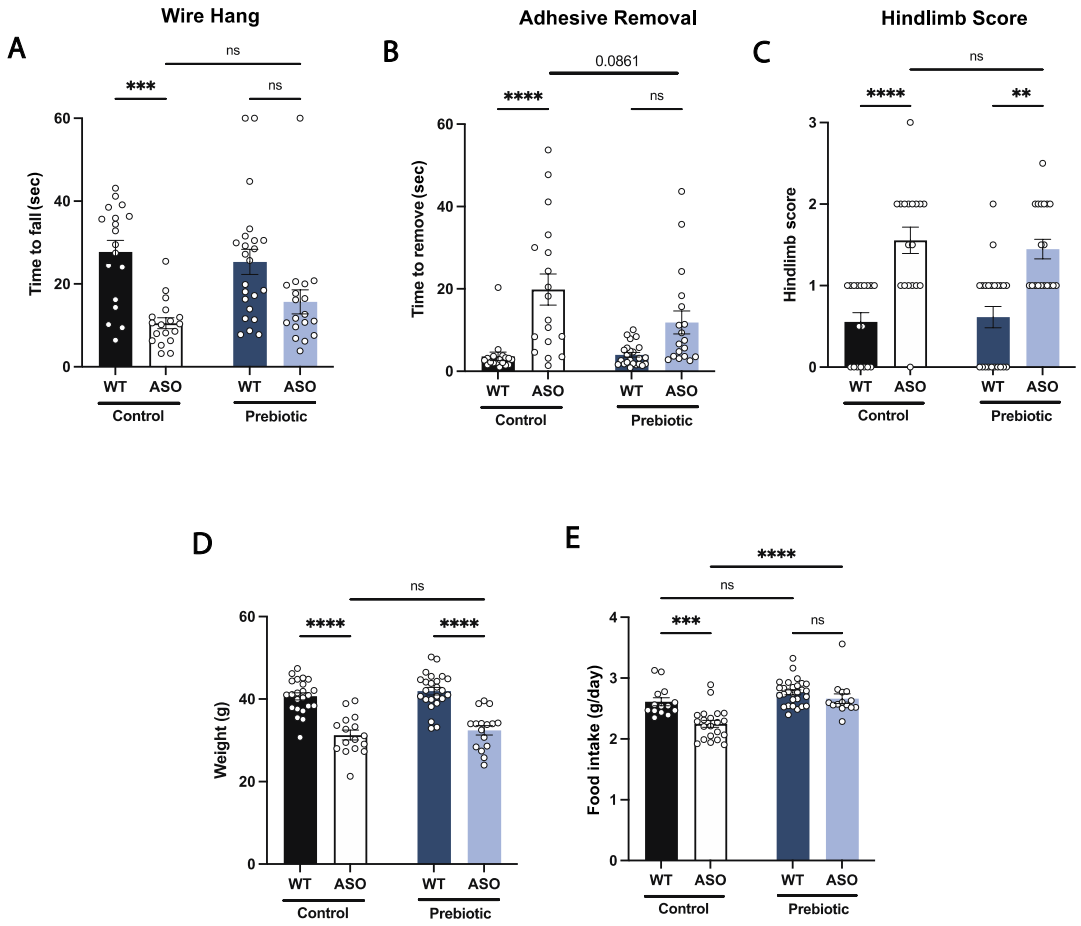

930 **Supplement Figure 3. Prebiotic diet does not improve performance in certain motor tests**
931 **A-C)** Motor behavior metrics for mice at 22 weeks from wire hang (A), adhesive removal (B),
932 and hindlimb score (C) tests (n=18-24/group). **D)** Mouse weight at 22 weeks (n=16-24/group).
933 **E)** Food intake per mouse recorded over the course of experiment. Data analyzed by two-way
934 ANOVA followed by Tukey's multiple comparisons test, except hindlimb score data, which was
935 analyzed by Kruskal-Wallis test. Bars represent mean ± SEM. *p<0.05, **p<0.01, ***p<0.001,
936 and ****p<0.0001.

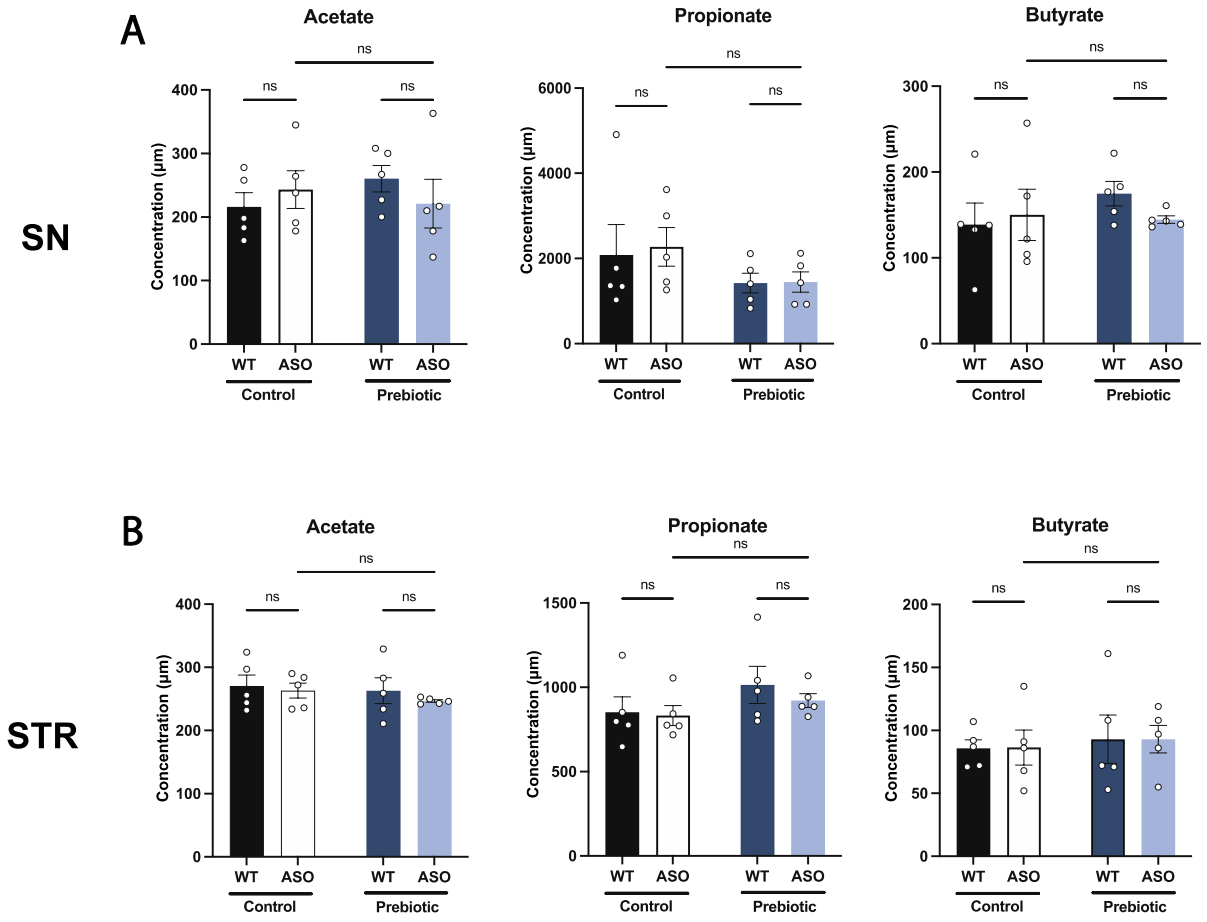

Supplement Figure 4. Prebiotics do not change SCFA levels in the brain

A,B) Concentration (µM) of acetate, propionate, and butyrate measured by UHP-LC in the substantia nigra (A) and striatum (B). Each point represents data from one mouse (n=5/group). Data analyzed by two-way ANOVA followed by Tukey's multiple comparisons test. Bars represent mean ± SEM.

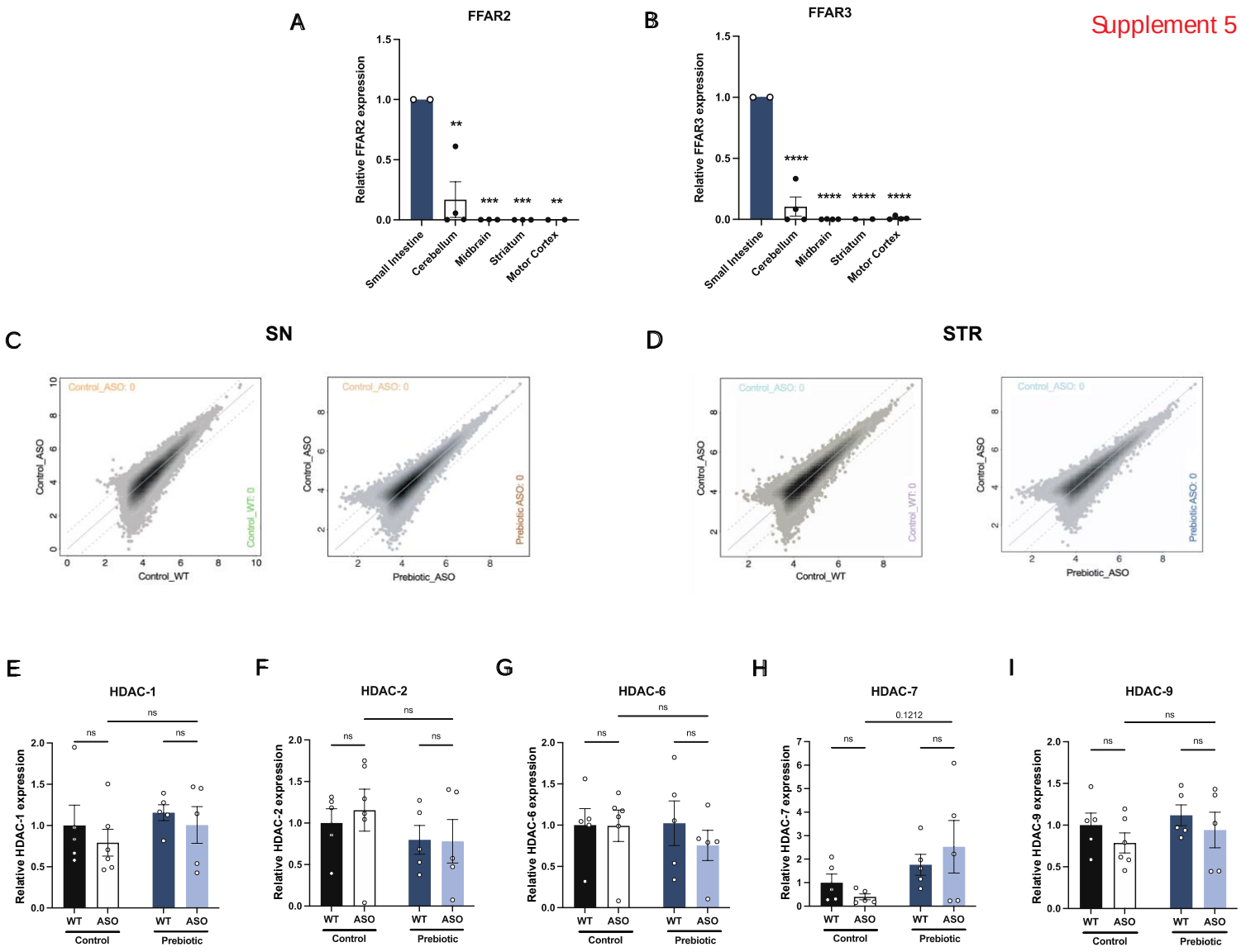

Supplement Figure 5. FFAR2/3 levels in brain and GI tissue and epigenetic analysis
A,B) qPCR measurement of FFAR2 (A) and FFAR3 (B) in small intestine, cerebellum, midbrain, striatum and motor cortex (n=2-4/group). **C,D)** ATAC-seq measurement of open chromatin regions in purified microglia in the substantia nigra (C) and striatum (D). **E-I)** qPCR measurement of HDAC-1 (E), HDAC-2 (F), HDAC-6 (G), HDAC-7 (H), and HDAC-9 (I) in the striatum (n=5-6/group). qPCR data analyzed by two-way ANOVA followed by Tukey's multiple comparisons test. Bars represent mean ± SEM. *p<0.05, **p<0.01, ***p<0.001, and ****p<0.0001.

Supplement 6

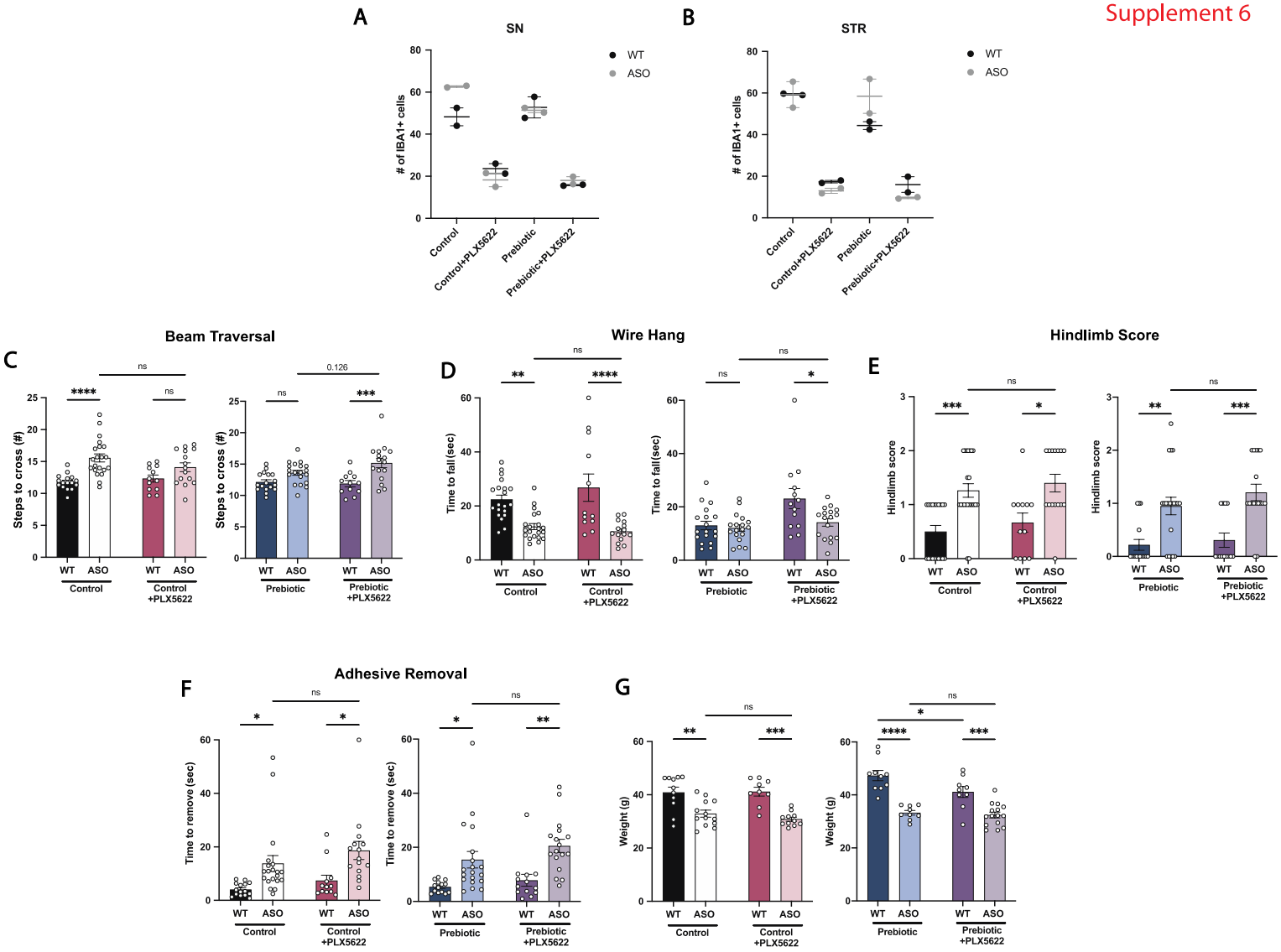

950 **Supplement Figure 6. Characterization of PLX5622 treatment**
951 **A,B)** Iba1+ cell count in the substantia nigra (A) and striatum (B). n=2/group. **C-F)** Motor
952 behavior metrics from beam traversal (C), wire hang (D), hindlimb score (E), and adhesive
953 removal (F) tests (n=12-23/group). **G)** Mouse weight at 22 weeks (n=9-15/group). Data analyzed
954 by two-way ANOVA followed by Tukey's multiple comparisons test. Bars represent mean ±
955 SEM. *p<0.05, **p<0.01, ***p<0.001, and ****p<0.0001.

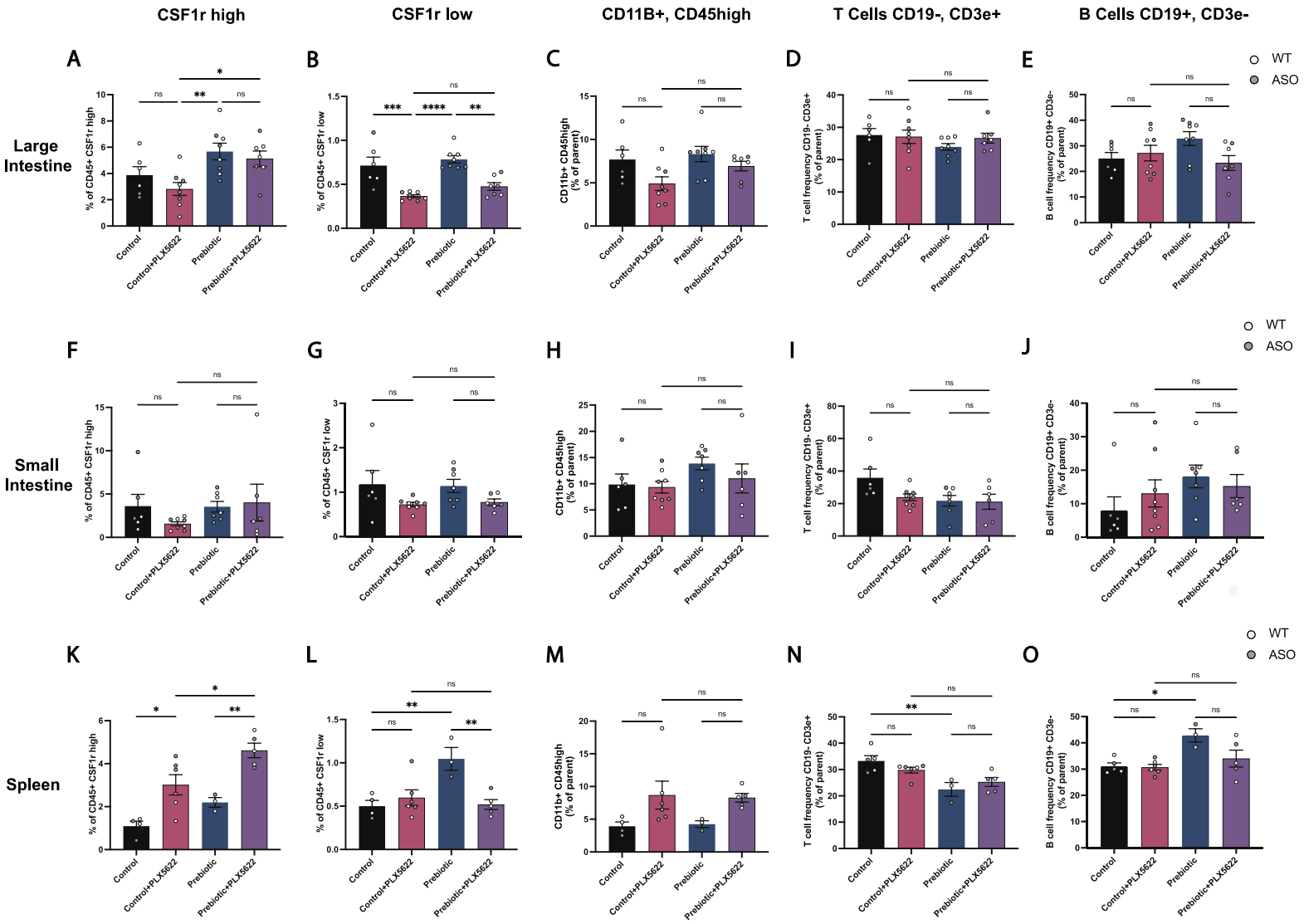

956 **Supplement Figure 7. Immune cell characterization in the gut and spleen of PLX5622-**
957 **treated mice**
958 **A-E)** Large intestine quantification of CD45, CSF1r+ high cells (A); CD45+, CSF1r low cells
959 (B); CD11b+, CD45 high cells (C); T cells (CD19-, CD3e+) (D); and B cells (CD19+, CD3e-)
960 (E). n=6-8/group. **F-J)** Small intestine quantification of the same populations (n=6-8/group). **K-**
961 **O)** Spleen quantification of the same populations (n=3-6/group). Each point represents data from
962 an individual mouse. White data points represent WT mice and grey data points represent ASO
963 mice. Data is combined from three independent experiments. Data analyzed by one-way
964 ANOVA followed by Tukey's multiple comparisons test. Bars represent mean ± SEM. *p<0.05,
965 **p<0.01, ***p<0.001, and ****p<0.0001.

966 **References**

967 Abdel-Haq, Reem, Johannes C. M. Schlachetzki, Christopher K. Glass, and Sarkis K.
968 Mazmanian. 2019. "Microbiome–Microglia Connections via the Gut–Brain Axis." *The*
969 *Journal of Experimental Medicine* 216 (1): 41–59.
970 Aho, Velma T. E., Madelyn C. Houser, Pedro A. B. Pereira, Jianjun Chang, Knut Rudi, Lars
971 Paulin, Vicki Hertzberg, Petri Auvinen, Malú G. Tansey, and Filip Scheperjans. 2021.
972 "Relationships of Gut Microbiota, Short-Chain Fatty Acids, Inflammation, and the Gut
973 Barrier in Parkinson's Disease." *Molecular Neurodegeneration* 16 (1): 6.
974 Alcalay, Roy N., Yian Gu, Helen Mejia-Santana, Lucien Cote, Karen S. Marder, and Nikolaos
975 Scarmeas. 2012. "The Association between Mediterranean Diet Adherence and
976 Parkinson's Disease." *Movement Disorders: Official Journal of the Movement Disorder*
977 *Society* 27 (6): 771–74.
978 Anderson, Sarah R., and Monica L. Vetter. 2019. "Developmental Roles of Microglia: A
979 Window into Mechanisms of Disease." *Developmental Dynamics: An Official*
980 *Publication of the American Association of Anatomists* 248 (1): 98–117.
981 Bachmann, C., J. P. Colombo, and J. Berüter. 1979. "Short Chain Fatty Acids in Plasma and
982 Brain: Quantitative Determination by Gas Chromatography." *Clinica Chimica Acta;*
983 *International Journal of Clinical Chemistry* 92 (2): 153–59.
984 Boulos, Christa, Nathalie Yaghi, Rita El Hayeck, Gessica Nha Heraoui, and Nicole Fakhoury-
985 Sayegh. 2019. "Nutritional Risk Factors, Microbiota and Parkinson's Disease: What Is
986 the Current Evidence?" *Nutrients* 11 (8). https://doi.org/10.3390/nu11081896.
987 Braak, Heiko, Kelly Del Tredici, Udo Rüb, Rob A. I. de Vos, Ernst N. H. Jansen Steur, and Eva
988 Braak. 2003. "Staging of Brain Pathology Related to Sporadic Parkinson's Disease."
989 *Neurobiology of Aging* 24 (2): 197–211.
990 Brodacki, Bogdan, Jacek Staszewski, Beata Toczyłowska, Ewa Kozłowska, Nadzieja Drela,
991 Małgorzata Chalimoniuk, and Adam Stepien. 2008. "Serum Interleukin (IL-2, IL-10, IL-
992 6, IL-4), TNFalpha, and INFgamma Concentrations Are Elevated in Patients with
993 Atypical and Idiopathic Parkinsonism." *Neuroscience Letters* 441 (2): 158–62.
994 Cait, A., M. R. Hughes, F. Antignano, J. Cait, P. A. Dimitriu, K. R. Maas, L. A. Reynolds, et al.
995 2018. "Microbiome-Driven Allergic Lung Inflammation Is Ameliorated by Short-Chain
996 Fatty Acids." *Mucosal Immunology* 11 (3): 785–95.

997 Çamcı, Gülşah, and Sıdıka Oğuz. 2016. "Association between Parkinson's Disease and
998 Helicobacter Pylori." *Journal of Clinical Neurology* 12 (2): 147–50.
999 Cantu-Jungles, Thaisa Moro, Andrea Caroline Ruthes, Marwa El-Hindawy, Roberta Barbara
1000 Moreno, Xiaowei Zhang, Lucimara M. C. Cordeiro, Bruce R. Hamaker, and Marcello
1001 Iacomini. 2018. "In Vitro Fermentation of Cookeina Speciosa Glucans Stimulates the
1002 Growth of the Butyrogenic Clostridium Cluster XIVa in a Targeted Way." *Carbohydrate*
1003 *Polymers* 183 (March): 219–29.
1004 Carroll, James A., Brent Race, Katie Williams, James Striebel, and Bruce Chesebro. 2018.
1005 "Microglia Are Critical in Host Defense against Prion Disease." *Journal of Virology* 92
1006 (15). https://doi.org/10.1128/JVI.00549-18.
1007 Casali, Brad T., Kathryn P. MacPherson, Erin G. Reed-Geaghan, and Gary E. Landreth. 2020.
1008 "Microglia Depletion Rapidly and Reversibly Alters Amyloid Pathology by Modification
1009 of Plaque Compaction and Morphologies." *Neurobiology of Disease* 142 (August):
1010 104956.
1011 Chan, James Chun Yip, Dorinda Yan Qin Kioh, Gaik Chin Yap, Bee Wah Lee, and Eric Chun
1012 Yong Chan. 2017. "A Novel LCMSMS Method for Quantitative Measurement of Short-
1013 Chain Fatty Acids in Human Stool Derivatized with 12C- and 13C-Labelled Aniline."
1014 *Journal of Pharmaceutical and Biomedical Analysis* 138 (May): 43–53.
1015 Chen, Szu-Ju, Chieh-Chang Chen, Hsin-Yu Liao, Ya-Ting Lin, Yu-Wei Wu, Jyh-Ming Liou,
1016 Ming-Shiang Wu, Ching-Hua Kuo, and Chin-Hsien Lin. 2022. "Association of Fecal and
1017 Plasma Levels of Short-Chain Fatty Acids With Gut Microbiota and Clinical Severity in
1018 Patients With Parkinson Disease." *Neurology* 98 (8): e848–58.
1019 Chesselet, Marie-Francoise, Franziska Richter, Chunni Zhu, Iddo Magen, Melanie B. Watson,
1020 and Sudhakar R. Subramaniam. 2012. "A Progressive Mouse Model of Parkinson's
1021 Disease: The Thy1-ASyn ('Line 61') Mice." *Neurotherapeutics: The Journal of the*
1022 *American Society for Experimental NeuroTherapeutics* 9 (2): 297–314.
1023 Choi, Jin Gyu, Namkwon Kim, In Gyoung Ju, Hyeyoon Eo, Su-Min Lim, Se-Eun Jang, Dong-
1024 Hyun Kim, and Myung Sook Oh. 2018. "Oral Administration of Proteus Mirabilis
1025 Damages Dopaminergic Neurons and Motor Functions in Mice." *Scientific Reports* 8 (1):
1026 1–13.

Cirstea, Mihai S., Adam C. Yu, Ella Golz, Kristen Sundvick, Daniel Kliger, Nina Radisavljevic, Liam H. Foulger, et al. 2020. "Microbiota Composition and Metabolism Are Associated With Gut Function in Parkinson's Disease." *Movement Disorders: Official Journal of the Movement Disorder Society* 35 (7): 1208–17.

Colombo, Alessio Vittorio, Rebecca Katie Sadler, Gemma Llovera, Vikramjeet Singh, Stefan Roth, Steffanie Heindl, Laura Sebastian Monasor, et al. 2021. "Microbiota-Derived Short Chain Fatty Acids Modulate Microglia and Promote Aβ Plaque Deposition." *ELife* 10 (April). https://doi.org/10.7554/eLife.59826.

Cui, Chun, Hui Hong, Yun Shi, Yu Zhou, Chen-Meng Qiao, Wei-Jiang Zhao, Li-Ping Zhao, et al. 2022. "Vancomycin Pretreatment on MPTP-Induced Parkinson's Disease Mice Exerts Neuroprotection by Suppressing Inflammation Both in Brain and Gut." *Journal of Neuroimmune Pharmacology: The Official Journal of the Society on NeuroImmune Pharmacology*, January. https://doi.org/10.1007/s11481-021-10047-y.

Das, Hiranmoy, Ajay Kumar, Zhiyong Lin, Willmar D. Patino, Paul M. Hwang, Mark W. Feinberg, Pradip K. Majumder, and Mukesh K. Jain. 2006. "Kruppel-like Factor 2 (KLF2) Regulates Proinflammatory Activation of Monocytes." *Proceedings of the National Academy of Sciences of the United States of America* 103 (17): 6653–58.

Datta, Moumita, Ori Staszewski, Elena Raschi, Maximilian Frosch, Nora Hagemeyer, Tuan Leng Tay, Thomas Blank, et al. 2018. "Histone Deacetylases 1 and 2 Regulate Microglia Function during Development, Homeostasis, and Neurodegeneration in a Context-Dependent Manner." *Immunity* 48 (3): 514-529.e6.

Deczkowska, Aleksandra, Hadas Keren-Shaul, Assaf Weiner, Marco Colonna, Michal Schwartz, and Ido Amit. 2018. "Disease-Associated Microglia: A Universal Immune Sensor of Neurodegeneration." *Cell* 173 (5): 1073–81.

Dorsey, E. Ray, Todd Sherer, Michael S. Okun, and Bastiaan R. Bloem. 2018. "The Emerging Evidence of the Parkinson Pandemic." *Journal of Parkinson's Disease* 8 (s1): S3–8.

Elmore, Monica R. P., Allison R. Najafi, Maya A. Koike, Nabil N. Dagher, Elizabeth E. Spangenberg, Rachel A. Rice, Masashi Kitazawa, et al. 2014. "Colony-Stimulating Factor 1 Receptor Signaling Is Necessary for Microglia Viability, Unmasking a Microglia Progenitor Cell in the Adult Brain." *Neuron* 82 (2): 380–97.

1057 Erny, Daniel, Nikolaos Dokalis, Charlotte Mezö, Angela Castoldi, Omar Mossad, Ori
1058 Staszewski, Maximilian Frosch, et al. 2021. “Microbiota-Derived Acetate Enables the
1059 Metabolic Fitness of the Brain Innate Immune System during Health and Disease.” *Cell*
1060 *Metabolism* 33 (11): 2260-2276.e7.
1061 Erny, Daniel, Anna Lena Hrabě de Angelis, Diego Jaitin, Peter Wieghofer, Ori Staszewski, Eyal
1062 David, Hadas Keren-Shaul, et al. 2015. “Host Microbiota Constantly Control Maturation
1063 and Function of Microglia in the CNS.” *Nature Neuroscience* 18 (7): 965–77.
1064 Fleming, Sheila M., Jonathan Salcedo, Pierre-Olivier Fernagut, Edward Rockenstein, Eliezer
1065 Masliah, Michael S. Levine, and Marie-Françoise Chesselet. 2004. “Early and
1066 Progressive Sensorimotor Anomalies in Mice Overexpressing Wild-Type Human α-
1067 Synuclein.” *The Journal of Neuroscience: The Official Journal of the Society for*
1068 *Neuroscience* 24 (42): 9434–40.
1069 Forsyth, Christopher B., Kathleen M. Shannon, Jeffrey H. Kordower, Robin M. Voigt, Maliha
1070 Shaikh, Jean A. Jaglin, Jacob D. Estes, Hemraj B. Dodiya, and Ali Keshavarzian. 2011.
1071 “Increased Intestinal Permeability Correlates with Sigmoid Mucosa Alpha-Synuclein
1072 Staining and Endotoxin Exposure Markers in Early Parkinson’s Disease.” *PloS One* 6
1073 (12): e28032.
1074 Frost, Gary, Michelle L. Sleeth, Meliz Sahuri-Arisoylu, Blanca Lizarbe, Sebastian Cerdan, Leigh
1075 Brody, Jelena Anastasovska, et al. 2014. “The Short-Chain Fatty Acid Acetate Reduces
1076 Appetite via a Central Homeostatic Mechanism.” *Nature Communications* 5 (April):
1077 3611.
1078 Furusawa, Yukihiro, Yuuki Obata, Shinji Fukuda, Takaho A. Endo, Gaku Nakato, Daisuke
1079 Takahashi, Yumiko Nakanishi, et al. 2013. “Commensal Microbe-Derived Butyrate
1080 Induces the Differentiation of Colonic Regulatory T Cells.” *Nature* 504 (7480): 446–50.
1081 Gao, Xiang, Honglei Chen, Teresa T. Fung, Giancarlo Logroscino, Michael A. Schwarzschild,
1082 Frank B. Hu, and Alberto Ascherio. 2007. “Prospective Study of Dietary Pattern and Risk
1083 of Parkinson Disease.” *The American Journal of Clinical Nutrition* 86 (5): 1486–94.
1084 Ge, Steven Xijin, Dongmin Jung, and Runan Yao. 2020. “ShinyGO: A Graphical Gene-Set
1085 Enrichment Tool for Animals and Plants.” *Bioinformatics* 36 (8): 2628–29.

George, Sonia, Nolwen L. Rey, Trevor Tyson, Corinne Esquibel, Lindsay Meyerdirk, Emily Schulz, Steven Pierce, et al. 2019. "Microglia Affect α-Synuclein Cell-to-Cell Transfer in a Mouse Model of Parkinson's Disease." *Molecular Neurodegeneration* 14 (1): 34.

Grabert, Kathleen, Tom Michoel, Michail H. Karavolos, Sara Clohisey, J. Kenneth Baillie, Mark P. Stevens, Tom C. Freeman, Kim M. Summers, and Barry W. McColl. 2016. "Microglial Brain Region-Dependent Diversity and Selective Regional Sensitivities to Aging." *Nature Neuroscience* 19 (3): 504–16.

Gratuze, Maud, Cheryl E. G. Leyns, and David M. Holtzman. 2018. "New Insights into the Role of TREM2 in Alzheimer's Disease." *Molecular Neurodegeneration* 13 (1): 66.

Hammond, Timothy R., Connor Dufort, Lasse Dissing-Olesen, Stefanie Giera, Adam Young, Alec Wysoker, Alec J. Walker, et al. 2019. "Single-Cell RNA Sequencing of Microglia throughout the Mouse Lifespan and in the Injured Brain Reveals Complex Cell-State Changes." *Immunity* 50 (1): 253-271.e6.

Hou, Yichao, Xingqi Li, Chang Liu, Ming Zhang, Xiaoying Zhang, Shaoyang Ge, and Liang Zhao. 2021. "Neuroprotective Effects of Short-Chain Fatty Acids in MPTP Induced Mice Model of Parkinson's Disease." *Experimental Gerontology* 150 (July): 111376.

Keren-Shaul, Hadas, Amit Spinrad, Assaf Weiner, Orit Matcovitch-Natan, Raz Dvir-Szternfeld, Tyler K. Ulland, Eyal David, et al. 2017. "A Unique Microglia Type Associated with Restricting Development of Alzheimer's Disease." *Cell* 169 (7): 1276-1290.e17.

Keshavarzian, Ali, Stefan J. Green, Phillip A. Engen, Robin M. Voigt, Ankur Naqib, Christopher B. Forsyth, Ece Mutlu, and Kathleen M. Shannon. 2015. "Colonic Bacterial Composition in Parkinson's Disease." *Movement Disorders: Official Journal of the Movement Disorder Society* 30 (10): 1351–60.

Kim, Hyeon Ju, Michael Rowe, Ming Ren, Jau-Shyong Hong, Po-See Chen, and De-Maw Chuang. 2007. "Histone Deacetylase Inhibitors Exhibit Anti-Inflammatory and Neuroprotective Effects in a Rat Permanent Ischemic Model of Stroke: Multiple Mechanisms of Action." *The Journal of Pharmacology and Experimental Therapeutics* 321 (3): 892–901.

Kim, Sangjune, Seung-Hwan Kwon, Tae-In Kam, Nikhil Panicker, Senthilkumar S. Karuppagounder, Saebom Lee, Jun Hee Lee, et al. 2019. "Transneuronal Propagation of

Pathologic α-Synuclein from the Gut to the Brain Models Parkinson's Disease." *Neuron* 103 (4): 627-641.e7.

Langmead, Ben, and Steven L. Salzberg. 2012. "Fast Gapped-Read Alignment with Bowtie 2." *Nature Methods* 9 (4): 357–59.

Lei, Fengyang, Naiwen Cui, Chengxin Zhou, James Chodosh, Demetrios G. Vavvas, and Eleftherios I. Paschalis. 2020. "CSF1R Inhibition by a Small-Molecule Inhibitor Is Not Microglia Specific; Affecting Hematopoiesis and the Function of Macrophages." *Proceedings of the National Academy of Sciences of the United States of America* 117 (38): 23336–38.

Ley, Ruth E., Peter J. Turnbaugh, Samuel Klein, and Jeffrey I. Gordon. 2006. "Microbial Ecology: Human Gut Microbes Associated with Obesity." *Nature* 444 (7122): 1022–23.

Li, Zhenzhen, Yanhui Jia, Shichao Han, Xingqin Wang, F. Han, Julei Zhang, Wei Zhang, H. Guan, and D. Hu. 2018. "Klf4 Alleviates Lipopolysaccharide-Induced Inflammation by Inducing Expression of MCP-1 Induced Protein 1 to Deubiquitinate TRAF6." *Cellular Physiology and Biochemistry: International Journal of Experimental Cellular Physiology, Biochemistry, and Pharmacology*. https://doi.org/10.1159/000491538.

Liu, Bojing, Fang Fang, Nancy L. Pedersen, Annika Tillander, Jonas F. Ludvigsson, Anders Ekbom, Per Svenningsson, Honglei Chen, and Karin Wirdefeldt. 2017. "Vagotomy and Parkinson Disease: A Swedish Register-Based Matched-Cohort Study." *Neurology* 88 (21): 1996–2002.

Liu, Jiaming, Fangyan Wang, Suzhi Liu, Jimei Du, Xuezhen Hu, Jiaojiao Xiong, Renchi Fang, Wenqian Chen, and Jing Sun. 2017. "Sodium Butyrate Exerts Protective Effect against Parkinson's Disease in Mice via Stimulation of Glucagon like Peptide-1." *Journal of the Neurological Sciences* 381 (October): 176–81.

Liu, Wenting, Sharmila Venugopal, Sana Majid, In Sook Ahn, Graciel Diamante, Jason Hong, Xia Yang, and Scott H. Chandler. 2020. "Single-Cell RNA-Seq Analysis of the Brainstem of Mutant SOD1 Mice Reveals Perturbed Cell Types and Pathways of Amyotrophic Lateral Sclerosis." *Neurobiology of Disease* 141 (July): 104877.

Luo, Yuheng, Ling Zhang, Hua Li, Hauke Smidt, André-Denis G. Wright, Keying Zhang, Xuemei Ding, et al. 2017. "Different Types of Dietary Fibers Trigger Specific Alterations

in Composition and Predicted Functions of Colonic Bacterial Communities in BALB/c Mice." *Frontiers in Microbiology* 8 (May): 966.

Magne, Fabien, Martin Gotteland, Lea Gauthier, Alejandra Zazueta, Susana Pesoa, Paola Navarrete, and Ramadass Balamurugan. 2020. "The Firmicutes/Bacteroidetes Ratio: A Relevant Marker of Gut Dysbiosis in Obese Patients?" *Nutrients* 12 (5). https://doi.org/10.3390/nu12051474.

Mallick, Himel, Ali Rahnavard, Lauren J. McIver, Siyuan Ma, Yancong Zhang, Long H. Nguyen, Timothy L. Tickle, et al. 2021. "Multivariable Association Discovery in Population-Scale Meta-Omics Studies." https://www.biorxiv.org/content/10.1101/2021.01.20.427420v1.

Menassa, David A., and Diego Gomez-Nicola. 2018. "Microglial Dynamics During Human Brain Development." *Frontiers in Immunology* 9 (May): 1014.

Molsberry, Samantha, Kjetil Bjornevik, Katherine C. Hughes, Brian Healy, Michael Schwarzschild, and Alberto Ascherio. 2020. "Diet Pattern and Prodromal Features of Parkinson Disease." *Neurology* 95 (15): e2095–2108.

Morais, Livia H., Henry L. Schreiber, and Sarkis K. Mazmanian. 2020. "The Gut Microbiota–Brain Axis in Behaviour and Brain Disorders." *Nature Reviews. Microbiology* 19 (4): 241–55.

Nissen, Jillian C., Kaitlyn K. Thompson, Brian L. West, and Stella E. Tsirka. 2018. "Csf1R Inhibition Attenuates Experimental Autoimmune Encephalomyelitis and Promotes Recovery." *Experimental Neurology* 307 (September): 24–36.

Onuska, Kate M. 2020. "The Dual Role of Microglia in the Progression of Alzheimer's Disease." *The Journal of Neuroscience: The Official Journal of the Society for Neuroscience*.

Parada Venegas, Daniela, Marjorie K. De la Fuente, Glauben Landskron, María Julieta González, Rodrigo Quera, Gerard Dijkstra, Hermie J. M. Harmsen, Klaas Nico Faber, and Marcela A. Hermoso. 2019. "Short Chain Fatty Acids (SCFAs)-Mediated Gut Epithelial and Immune Regulation and Its Relevance for Inflammatory Bowel Diseases." *Frontiers in Immunology* 10 (March): 277.

Poewe, Werner, Klaus Seppi, Caroline M. Tanner, Glenda M. Halliday, Patrik Brundin, Jens Volkmann, Anette-Eleonore Schrag, and Anthony E. Lang. 2017. "Parkinson Disease." *Nature Reviews Disease Primers* 3 (1): 1–21.

Pu, Yaoyu, Lijia Chang, Youge Qu, Siming Wang, Kai Zhang, and Kenji Hashimoto. 2019. "Antibiotic-Induced Microbiome Depletion Protects against MPTP-Induced Dopaminergic Neurotoxicity in the Brain." *Aging* 11 (17): 6915–29.

Reale, M., C. Iarlori, A. Thomas, D. Gambi, B. Perfetti, M. Di Nicola, and M. Onofrj. 2009. "Peripheral Cytokines Profile in Parkinson's Disease." *Brain, Behavior, and Immunity* 23 (1): 55–63.

Rockenstein, Edward, Margaret Mallory, Makoto Hashimoto, David Song, Clifford W. Shults, Ingrid Lang, and Eliezer Masliah. 2002. "Differential Neuropathological Alterations in Transgenic Mice Expressing Alpha-Synuclein from the Platelet-Derived Growth Factor and Thy-1 Promoters." *Journal of Neuroscience Research* 68 (5): 568–78.

Sadler, Rebecca, Julia V. Cramer, Steffanie Heindl, Sarantos Kostidis, Dene Betz, Kielen R. Zuurbier, Bernd H. Northoff, et al. 2020. "Short-Chain Fatty Acids Improve Poststroke Recovery via Immunological Mechanisms." *The Journal of Neuroscience: The Official Journal of the Society for Neuroscience* 40 (5): 1162–73.

Sampson, Timothy R., Collin Challis, Neha Jain, Anastasiya Moiseyenko, Mark S. Ladinsky, Gauri G. Shastri, Taren Thron, et al. 2020. "A Gut Bacterial Amyloid Promotes α-Synuclein Aggregation and Motor Impairment in Mice." *ELife* 9 (February). https://doi.org/10.7554/eLife.53111.

Sampson, Timothy R., Justine W. Debelius, Taren Thron, Stefan Janssen, Gauri G. Shastri, Zehra Esra Ilhan, Collin Challis, et al. 2016. "Gut Microbiota Regulate Motor Deficits and Neuroinflammation in a Model of Parkinson's Disease." *Cell* 167 (6): 1469-1480.e12.

Scheperjans, Filip, Velma Aho, Pedro A. B. Pereira, Kaisa Koskinen, Lars Paulin, Eero Pekkonen, Elena Haapaniemi, et al. 2015. "Gut Microbiota Are Related to Parkinson's Disease and Clinical Phenotype." *Movement Disorders: Official Journal of the Movement Disorder Society* 30 (3): 350–58.

Shin, Na-Ri, Tae Woong Whon, and Jin-Woo Bae. 2015. "Proteobacteria: Microbial Signature of Dysbiosis in Gut Microbiota." *Trends in Biotechnology* 33 (9): 496–503.

Silva, Ygor Parladore, Andressa Bernardi, and Rudimar Luiz Frozza. 2020. "The Role of Short-Chain Fatty Acids From Gut Microbiota in Gut-Brain Communication." *Frontiers in Endocrinology* 11 (January): 25.

Spangenberg, Elizabeth E., Rafael J. Lee, Allison R. Najafi, Rachel A. Rice, Monica R. P. Elmore, Mathew Blurton-Jones, Brian L. West, and Kim N. Green. 2016. "Eliminating Microglia in Alzheimer's Mice Prevents Neuronal Loss without Modulating Amyloid-β Pathology." *Brain: A Journal of Neurology* 139 (4): 1265–81.

Spangenberg, Elizabeth, Paul L. Severson, Lindsay A. Hohsfield, Joshua Crapser, Jiazhong Zhang, Elizabeth A. Burton, Ying Zhang, et al. 2019. "Sustained Microglial Depletion with CSF1R Inhibitor Impairs Parenchymal Plaque Development in an Alzheimer's Disease Model." *Nature Communications* 10 (1): 1–21.

Svensson, Elisabeth, Erzsébet Horváth-Puhó, Reimar W. Thomsen, Jens Christian Djurhuus, Lars Pedersen, Per Borghammer, and Henrik Toft Sørensen. 2015. "Vagotomy and Subsequent Risk of Parkinson's Disease." *Annals of Neurology* 78 (4): 522–29.

Tan, Ai Huey, Sanjiv Mahadeva, Abdul Malik Thalha, Peter R. Gibson, Chiun Khang Kiew, Chia Ming Yeat, Sheang Wen Ng, et al. 2014. "Small Intestinal Bacterial Overgrowth in Parkinson's Disease." *Parkinsonism & Related Disorders* 20 (5): 535–40.

Tan, Yun-Long, Yi Yuan, and Li Tian. 2020. "Microglial Regional Heterogeneity and Its Role in the Brain." *Molecular Psychiatry* 25 (2): 351–67.

Thion, Morgane Sonia, Donovan Low, Aymeric Silvin, Jinmiao Chen, Pauline Grisel, Jonas Schulte-Schrepping, Ronnie Blecher, et al. 2018. "Microbiome Influences Prenatal and Adult Microglia in a Sex-Specific Manner." *Cell* 172 (3): 500-516.e16.

Troncoso-Escudero, Paulina, Alejandra Parra, Melissa Nassif, and Rene L. Vidal. 2018. "Outside in: Unraveling the Role of Neuroinflammation in the Progression of Parkinson's Disease." *Frontiers in Neurology* 9 (October): 860.

Turnbaugh, Peter J., Vanessa K. Ridaura, Jeremiah J. Faith, Federico E. Rey, Rob Knight, and Jeffrey I. Gordon. 2009. "The Effect of Diet on the Human Gut Microbiome: A Metagenomic Analysis in Humanized Gnotobiotic Mice." *Science Translational Medicine* 1 (6): 6ra14.

Unger, Marcus M., Jörg Spiegel, Klaus-Ulrich Dillmann, David Grundmann, Hannah Philippeit, Jan Bürmann, Klaus Faßbender, Andreas Schwiertz, and Karl-Herbert Schäfer. 2016. "Short Chain Fatty Acids and Gut Microbiota Differ between Patients with Parkinson's Disease and Age-Matched Controls." *Parkinsonism & Related Disorders* 32 (November): 66–72.

1239 Vichaya, Elisabeth G., Sajida Malik, Luba Sominsky, Bianca G. Ford, Sarah J. Spencer, and
1240 Robert Dantzer. 2020. "Microglia Depletion Fails to Abrogate Inflammation-Induced
1241 Sickness in Mice and Rats." *Journal of Neuroinflammation* 17 (1): 172.
1242 Vieira, Erica L. M., Alda J. Leonel, Alexandre P. Sad, Nathália R. M. Beltrão, Thaís F. Costa,
1243 Talita M. R. Ferreira, Ana C. Gomes-Santos, et al. 2012. "Oral Administration of Sodium
1244 Butyrate Attenuates Inflammation and Mucosal Lesion in Experimental Acute Ulcerative
1245 Colitis." *The Journal of Nutritional Biochemistry* 23 (5): 430–36.
1246 Villa, Alessandro, Paolo Gelosa, Laura Castiglioni, Mauro Cimino, Nicoletta Rizzi, Giovanna
1247 Pepe, Federica Lolli, et al. 2018. "Sex-Specific Features of Microglia from Adult Mice."
1248 *Cell Reports* 23 (12): 3501–11.
1249 Vinolo, Marco A. R., Hosana G. Rodrigues, Renato T. Nachbar, and Rui Curi. 2011. "Regulation
1250 of Inflammation by Short Chain Fatty Acids." *Nutrients* 3 (10): 858–76.
1251 Wallen, Zachary D., William J. Stone, Stewart A. Factor, Eric Molho, Cyrus P. Zabetian, David
1252 G. Standaert, and Haydeh Payami. 2021. "Exploring Human-Genome Gut-Microbiome
1253 Interaction in Parkinson's Disease." *NPJ Parkinson's Disease* 7 (1): 74.
1254 Watson, Melanie B., Franziska Richter, Soo Kyung Lee, Lauryn Gabby, Jennifer Wu, Eliezer
1255 Masliah, Rita B. Effros, and Marie-Françoise Chesselet. 2012. "Regionally-Specific
1256 Microglial Activation in Young Mice over-Expressing Human Wildtype Alpha-
1257 Synuclein." *Experimental Neurology* 237 (2): 318–34.
1258 Weng, Cheng-Yu, Ting-Hao Kuo, Laura Min Xuan Chai, Hsin-Bai Zou, Tzu-Hsuan Feng, Yun-
1259 Ju Huang, Jemmy C. Tsai, et al. 2020. "Rapid Quantification of Gut Microbial Short-
1260 Chain Fatty Acids by PDART-MS." *Analytical Chemistry* 92 (22): 14892–97.
1261 Wolf, F. Alexander, Philipp Angerer, and Fabian J. Theis. 2018. "SCANPY: Large-Scale Single-
1262 Cell Gene Expression Data Analysis." *Genome Biology* 19 (1): 15.
1263 Wu, Gary D., Jun Chen, Christian Hoffmann, Kyle Bittinger, Ying-Yu Chen, Sue A. Keilbaugh,
1264 Meenakshi Bewtra, et al. 2011. "Linking Long-Term Dietary Patterns with Gut Microbial
1265 Enterotypes." *Science* 334 (6052): 105–8.
1266 Yang, Dongming, Deming Zhao, Syed Zahid Ali Shah, Wei Wu, Mengyu Lai, Xixi Zhang, Jie
1267 Li, et al. 2019. "The Role of the Gut Microbiota in the Pathogenesis of Parkinson's
1268 Disease." *Frontiers in Neurology* 10 (November): 1155.

1269 Yang, Xiaoxia, Honglei Ren, Kristofer Wood, Minshu Li, Shenfeng Qiu, Fu-Dong Shi, Cungen
1270 Ma, and Qiang Liu. 2018. “Depletion of Microglia Augments the Dopaminergic
1271 Neurotoxicity of MPTP.” *FASEB Journal: Official Publication of the Federation of*
1272 *American Societies for Experimental Biology* 32 (6): 3336–45.
1273 Zhu, Qiyun, Shi Huang, Antonio Gonzalez, Imran McGrath, Daniel McDonald, Niina Haiminen,
1274 George Armstrong, et al. 2021. “OGUs Enable Effective, Phylogeny-Aware Analysis of
1275 Even Shallow Metagenome Community Structures.” bioRxiv.
1276 https://www.biorxiv.org/content/10.1101/2021.04.04.438427v1.
1277 Zhu, Qiyun, Uyen Mai, Wayne Pfeiffer, Stefan Janssen, Francesco Asnicar, Jon G. Sanders,
1278 Pedro Belda-Ferre, et al. 2019. “Phylogenomics of 10,575 Genomes Reveals
1279 Evolutionary Proximity between Domains Bacteria and Archaea.” *Nature*
1280 *Communications* 10 (1): 5477.